Polymer Engineering & Science

WILEY | spe INSPIRING PLASTICS PROFESSIONALS

RESEARCH ARTICLE OPEN ACCESS

Comprehensive Surrogate Models for Predicting the Melt Conveying Characteristics of Channel Segments in High-Performance Single-Screw Extruders

Daniel Herzog[1] | Wolfgang Roland[2] | Christian Marschik[3] | Gerald Berger-Weber[1]

[1]Institute of Polymer Processing and Digital Transformation, Johannes Kepler University Linz, Linz, Austria | [2]Private Collaborator | [3]Competence Center CHASE GmbH, Linz, Austria

Correspondence: Daniel Herzog (daniel.herzog@jku.at)

Received: 13 August 2025 | **Revised:** 2 October 2025 | **Accepted:** 11 October 2025

Funding: This work was supported by the Austrian Science Fund (FWF) (10.55776/I4872), and COMET Center CHASE, Austrian Research Promotion Agency (FFG).

Keywords: curvature | flow simulation | hybrid modeling | polymer extrusion | power-law fluid | representative shear rate

ABSTRACT

Plastics converters are increasingly considering high-performance screws in single-screw extrusion to meet demanding production requirements. In this context, reliable prediction models for melt conveying support the search for optimum designs without exhaustive experimental trials. Although full-scale fluid dynamics simulations would closely represent the process, their high computational effort is rarely affordable in an industrial setting. Conversely, fast-computing extruder calculations using surrogate models fail to capture the influence of channel curvature in multi-flighted screw segments, thus becoming inaccurate for high-performance screws. To overcome these limitations, we developed generic dimensionless analytical equations for the local pumping capability, viscous dissipation, and average shear rate in metering channels. First, a comprehensive simulation database for the flow of power-law fluids through confined curved channel segments was generated that covers a vast range of designs and process configurations in single-screw extrusion. Subsequently, this database was approximated by continuous functions using knowledge-guided symbolic regression. The resulting characteristic equations excellently forecast the simulations throughout the entire design space with less than 3.5% average deviation, significantly outperforming existing approximations. When implemented in segmented extrusion calculations, these surrogate models enable quick and reliable statements on melt conveying in both conventional and high-performance extruders for more efficient screw design and troubleshooting.

1 | Introduction

Single-screw extruders play a prominent role in polymer processing across the whole product value chain: They are integrated into continuous extrusion lines for pipe, profile, film and sheet production, post-reactor processing, and polymer recycling [1]. In any case, the extruder must supply the polymer in molten state for the subsequent shaping processes in sufficient quality and quantity. For reaching the desired output, sufficient pressure has to be generated along the melt conveying zone to overcome the flow resistance of the downstream equipment. Simultaneously, the dissipated energy into the polymer melt should be minimized to prevent the material from degrading at high temperatures, and to reduce the environmental impact of the extrusion process. More intense global competition and dedication to sustainable development goals steadily increase the requirements on both pumping capability and energy efficiency of single-screw extruders for a broadening spectrum of plastic compounds, including recycled or bio-based grades with fluctuating properties. These requirements can no longer be fully met

Summary

- Three-dimensional flow of power-law fluids in helical screw channels.
- Comprehensive parametric study with generic solution strategy.
- Fully independent consideration of curvature and flight effects.
- Representative shear rate based on complete flow field.
- Analytical screw characteristic curves with extended range of application.

with traditional extruder screw designs, prompting manufacturers to resort to high-performance variants.

Over the last seven decades, various high-performance screw designs have been proposed to expand the boundaries of single-screw extrusion. Barrier screws enable enhanced plastication rates by introducing a barrier flight that is undercut to the main flight. The flight undercut is dimensioned to attain faster melt removal while separating molten from solid polymer. The cross-sections of the solid- and melt-conveying channels gradually shrink and expand, respectively, to ensure continuous melt transport across the barrier flight [2]. Improving both melting and mixing capability is possible by employing wave-dispersion screws: These screws are characterized by two parallel channels that are alternately oscillating in depth, as well as by undercut flights that also allow solid particles to cross [1]. This causes repetitive splitting of the flow and passage though tight cross-sections, contributing to better homogenization, dispersion of fillers, and accelerated melting due to early breakup of the solid bed [3]. The adjacent shallow and deep channel sections in both barrier and wave screws simultaneously favor high output stability and low energy demand. A comprehensive discussion of high-performance screws is given by Campbell and Spalding [3], Rauwendaal [2] and Chung [1]. All these expected improvements, however, are only realized with an intelligent screw design [1]. Due to their complex channel shapes, the melt flow in high-performance screws is still poorly understood, and optimizing their design usually requires exhaustive experimental trials. Hence, fast and reliable prediction models for pumping capability and viscous dissipation can reduce development costs and facilitate the implementation of high-performance screws in industry.

The pioneering attempts to model the melt conveying performance of screw pumps were taken by Rowell and Finlayson [4, 5], considering the isothermal down-channel flow of Newtonian fluids between parallel plates. Their design equations were adopted by Carley et al. [6] for polymer extrusion and supplemented by Mohr and Mallouk [7] with a mathematical description of the transverse flow. Booy [8] further included the effect of channel curvature on the flow rate and power requirements of single-screw extruders. These early theories provide exact analytical solutions for the melt conveying characteristics as a linear superposition of three flow components: (i) a drag-induced flow, (ii) a pressure-driven flow, and (iii) a transverse flow. However, polymer melts usually exhibit shear thinning behavior, which causes a coupling of the flow components due to the shear-rate-dependent viscosity. Especially for commodity polymers, these coupling effects strongly affect the flow field. Thus, consistently accurate predictions cannot be expected from these analytical solutions.

Since the coupled flow problem for shear thinning melts can no longer be solved analytically, numerical methods are required to obtain realistic results. Using the shooting method, Zamodits and Pearson [9] computed pumping characteristics for power-law fluids in flattened channels, taking both down-channel and transverse flow into account. Roland et al. [10] refined the approach by considering curvature effects on both pumping capability and viscous dissipation. Thanks to continued advances in computing power and resources, it is now possible to solve for the complete three-dimensional flow pattern of non-Newtonian fluids in the curved screw channel. Melt conveying characteristics based on this information were computed, for instance, by Lim et al. [11] using finite elements, and by Herzog et al. [12] using finite volumes. These sophisticated models already provide a close and detailed representation of the real flow conditions inside the extruder. However, such simulations still take several hours on standard office workstations to evaluate a single design point; and they require domain experts and software licenses for proper execution. As a result, fully three-dimensional simulations quickly become computationally too expensive for screw design or troubleshooting tasks.

Aiming for satisfactory alternatives to purely analytical or numerical approaches, several researchers have proposed analytical regression models for melt conveying based on computational extrusion data. Since the initial expressions by Potente [13], which are valid only for shallow metering zones in a tight operating range, the numerical databases have been successively refined and extended to yield more generally applicable models. Major advancements concerned incorporating the effect of the screw flights [14–16], and augmenting the data space towards strongly overridden zones, larger pitches, and narrower channels in high-performance screws [17]. Herzog et al. [12] further managed to evolve expressions that capture the flow conditions in three-dimensional curved channels. To date, these curved channel models mimic the behavior of single-flighted metering zones of single-screw extruders most closely.

When applied to high-performance screws, however, even the most advanced regression models still miss important aspects. The models by Marschik et al. [17], for instance, ignore channel curvature, giving rise to prediction errors in the range of 20%–40% for deep channels with depth-to-diameter ratios $h/D > 0.1$ [12, 18]. In high-performance extruders, such channels typically extend over a large portion of the screw length and thus strongly influence the overall conveying performance. The expressions by Herzog et al. [12], in contrast, are tuned exclusively to single-flighted screw channels with aperture angles above 300 degrees. Due to the limited scope of the training samples, these expressions become unreliable for multi-flighted screws with aperture angles that are several times narrower, where the influence of the screw flights on the flow is much more pronounced. Hence, generally valid prediction models for high-performance screws need to cover highly curved and boxy channels at the same time.

Another weakness of the existing regression models is their reliance on the power-law model for polymer melt viscosity. The power-law model fails to capture the rheological behavior in the transitional shear rate regime, which is observed for several polymers in deep metering channels of single-screw extruders. Although representative power-law parameters can be iteratively computed from more sophisticated rheological models, as described in [19, 20], the accuracy of the values obtained highly depends on the choice of the representative shear rate. Since the representative shear rate is calculated without considering curvature and flight effects in both cases, the local power-law parameters become highly uncertain in the transitional regime, especially when evaluated for deep or narrow channels in high-performance screws. Shear rate models based on the complete three-dimensional flow field would provide more realistic estimates for the viscosity parameters, minimizing a critical source of error for extruder performance calculations.

This paper presents more universally applicable regression models for predicting the local pumping capability, viscous dissipation, and representative shear rate of metering channels in single-screw extruders. These models fully consider three-dimensional curvature effects alongside the shear thinning behavior over a comprehensive operating range for both conventional and high-performance screws, thus overcoming the limitations of existing approximations. When implemented in segmented extruder calculations, they can significantly shorten development times due to lower demand for time-consuming, full-scale numerical simulations. For the derivation of the models, we adopted a hybrid modeling approach introduced in [21], which is described in the remainder of this paper: Section 2 revisits the mathematical problem formulation from our previous contribution [12] and defines the parametric design study for data collection. Section 3 explains the generic numerical solution strategy for the parametric study and showcases new insights into the effects of channel curvature on melt conveying. Section 4 describes the regression procedure used to approximate the simulation data and assesses the prediction quality of the models obtained. Finally, we summarize the key improvements of our new models and suggest routes for their successful application.

2 | Physical Problem

2.1 | Flow Domain

Single-screw extruders transport the polymer melt within helical channels, as schematically depicted in Figure 1a for an exemplary double-flighted screw. These channels are bounded by the cylindrical surfaces of the screw shaft and the surrounding barrel, and by the twisted flanks of the screw flights. To reduce the complexity of the modeling task, this study focuses on short segments of individual channels with constant dimensions along the screw-barrel axis. The cross-sectional

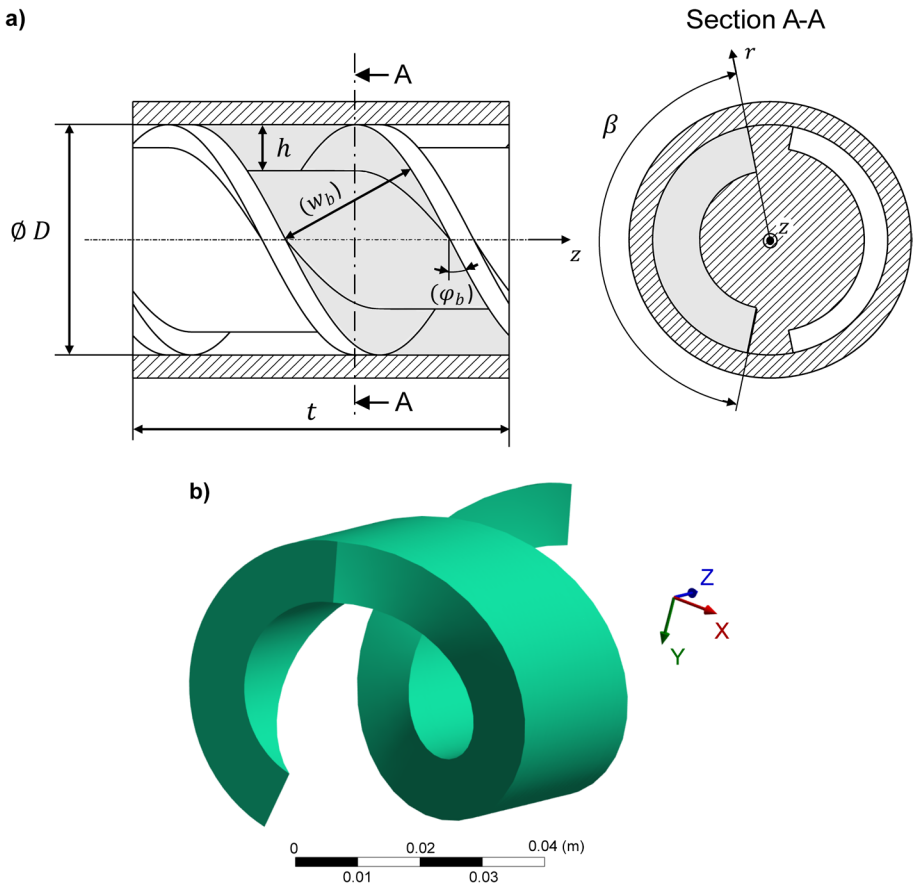

FIGURE 1 | (a) Schematic sketch of a high-performance single-screw extruder segment, with one particular channel highlighted in gray. (b) Three-dimensional flow domain of a confined helical channel segment.

shape of the screw channel is further simplified by omitting small structural features like radii, flight taper, and the radial clearance between flight tip and barrel. The resulting computational flow domain for one full revolution (Figure 1b) is uniquely defined by the following parameters: (i) the barrel diameter D, (ii) the channel depth h, (iii) the screw pitch t, and (iv) the aperture angle β along the circumference. The pitch angle φ, channel width w, and down-channel length per revolution Z are determined by these parameters and the radial distance from the screw axis:

$$\varphi(r) = \arctan\left(\frac{t}{2\,\pi\,r}\right); \tag{1}$$

$$w(r) = \beta\, r\, \sin\varphi(r) = \beta\, r\, \frac{t}{\sqrt{(2\,\pi\,r)^2 + t^2}}; \tag{2}$$

$$Z(r) = \frac{t}{\sin\varphi(r)} = \sqrt{(2\,\pi\,r)^2 + t^2}. \tag{3}$$

The subscript "b" in Figure 1 refers to the inner barrel surface ($r = D/2$). The cross-sectional area ΔA covered by the flight radii can be considered retrospectively, on average, by a correction term for the outer channel width:

$$w_{b,\mathrm{eff}} = w_b - \frac{B_a + B_p}{h} \tag{4}$$

as suggested by Potente [22]. However, three-dimensional numerical simulations by Spalding et al. [23] revealed that the pumping capability in the melt conveying section remained almost unaffected by the flight radii of up to 2.5 times the channel depth. Consequently, the absence of the flight radii in the simulations is expected to be uncritical for prediction accuracy.

Neglecting the flight clearance, in contrast, needs to be seriously questioned in the case of high-performance screws, which exhibit selectively undercut flights to promote leakage flow. Depending on the size of the undercut and the local pressure gradient, this leakage flow may affect the channel flow rates by several dozen percent. Moreover, the leakage gap allows for the exchange of material between different channel segments, which additionally influences the local melt temperature. Being directly coupled with the pumping characteristics of both neighboring channels, full consideration of the leakage flow would require a larger flow domain spanning the entire circumference, which largely complicates the numerical calculations. For the sake of simplicity, we thus decided to model the channel flow separately from the leakage flow at the local level. The interaction between local channel and leakage flows can still be considered on the entire screw zone level, for instance, by a flow network model demonstrated in [24]. Regression models for the melt conveying characteristics in the flight clearance have already been provided by Marschik et al.

2.2 | Governing Equations

For computing the flow characteristics of interest, the conservation equations for mass, momentum, and energy must be solved alongside proper constitutive relations and boundary conditions. The segregated consideration of individual channels allows for adopting the framework from our previous study [12] for single-flighted screws, making the following simplifying assumptions:

- The flow is steady, laminar, and fully developed.
- The polymer melt temperature is uniform.
- Body forces, such as inertia or gravity, can be ignored.
- The flow is viewed from a rotating frame of reference attached to the screw. From this perspective, the screw is at rest, and the barrel rotates in the opposite direction.
- The polymer melt is incompressible, purely viscous, and wall-adhering. The shear-rate-dependent viscosity η is described by a power law according to Ostwald and deWaele [25, 26]

$$\eta = K\,[2\,\boldsymbol{D}{:}\boldsymbol{D}]^{(n-1)/2} \tag{5}$$

with $\boldsymbol{D}$ as the three-dimensional rate-of-deformation tensor, K as power-law consistency, and n as power-law index.

As discussed in [12], body forces are negligible in polymer extrusion compared to viscous forces, which is reflected by Reynolds and Galilei numbers below 10^{-2}. This also implies equivalent flow rates, dissipation rates, and local deformation rates in a stationary reference frame and a reference frame rotating with the screw [12, 27]. Reported differences for these variables between the cases of rotating screw and rotating barrel can be explained by the following reasons: (i) the unwrapping of the channel in calculations, which erroneously assumes a translational motion between the parts, or (ii) flow conditions where inertia plays a significant role. Assuming isothermal conditions is also justified for short channel segments, as temperature changes in the main flow direction are limited and dominate cross-sectional temperature variations in polymer melt flows [28]. The assumptions of fully developed flow and an inelastic fluid, in contrast, need to be readdressed for high-performance screws: These screws contain several tapered channel sections, where the melt streams are intentionally rearranged and the polymer is subjected to elongational flow. Yet the taper angles in high-performance screws are typically smaller than 10° over a large part of the screw length, keeping the elongation rates small compared to the viscous shear rates. Even for a strongly convergent wave-dispersion zone under high-speed extrusion conditions, the shear rates surpass the elongation rates by roughly one decade as revealed by an analytical estimation provided in Supplementary File S1. This recognition is also reflected in the widely used lubrication approximation in polymer extrusion. As viscoelastic and chaotic flow problems are difficult to solve, the sacrificed accuracy is clearly outweighed by the reduced computational effort and less complex design space for model development.

The following equations then apply in the interior of the flow domain:

$$\nabla \cdot \boldsymbol{v} = 0 \qquad \text{(conservation of mass)}, \tag{6}$$

$$\nabla p = \nabla \cdot \boldsymbol{\tau} \qquad \text{(conservation of momentum)}, \tag{7}$$

$$\boldsymbol{\tau} = 2\,\eta\,\boldsymbol{D} = \eta\left[\nabla \boldsymbol{v} + (\nabla \boldsymbol{v})^T\right] \qquad \text{(constitutive relation)}, \tag{8}$$

for the relative flow velocity $\boldsymbol{v}$, the melt pressure p, and the viscous stress tensor $\boldsymbol{\tau}$. Energy conservation is automatically implied by Equations (6) and (7).

The boundary conditions on the part surfaces are, with respect to the moving reference frame, stagnation at the screw -

$$\boldsymbol{v_c} = \boldsymbol{v_a} = \boldsymbol{v_p} = \boldsymbol{0} \tag{9}$$

- and clockwise rotation at angular speed ω in circumferential direction $\boldsymbol{e_\vartheta}$ at the barrel:

$$\boldsymbol{v_b} = \omega\,\frac{D}{2}\,\boldsymbol{e_\vartheta}\,. \tag{10}$$

In our simulation model, the kinematic boundary condition (10) is imposed on the cylindrical barrel surface as positive angular velocity ω with the axis of rotation pointing in positive extrusion direction $\boldsymbol{e_z}$.

At the inlet and outlet sections, identical velocity distributions are prescribed -

$$v_{\text{in}} = v_{\text{out}} \tag{11}$$

- alongside the volumetric flow rate $\dot{V}$ or average axial pressure gradient p' between both boundaries, depending on the selected design point (see Section 2.4):

$$\dot{V} = \iint \boldsymbol{v} \cdot \boldsymbol{e_z}\,\mathrm{d}A, \tag{12}$$

$$\frac{p_{\text{out}} - p_{\text{in}}}{t} = p', \tag{13}$$

with $\boldsymbol{e_z}$ as unit vector in axial direction. The unknown counterpart of these two quantities is evaluated as an output parameter. Further output parameters of interest are the viscous dissipation rate

$$\dot{W}_{\text{diss}} = \iiint \boldsymbol{\tau}\!:\!(\nabla \boldsymbol{v})\,\mathrm{d}V = \iiint 2\,\eta\,\boldsymbol{D}\!:\!\boldsymbol{D}\,\mathrm{d}V = \iiint K\,(2\,\boldsymbol{D}\!:\!\boldsymbol{D})^{\frac{n+1}{2}}\,\mathrm{d}V, \tag{14}$$

and the mechanical power consumption within the channel segment

$$P_{\text{mech}} = \oiint (\boldsymbol{\tau} \cdot \boldsymbol{e_r}) \cdot \boldsymbol{v_b}\,\mathrm{d}S_b, \tag{15}$$

with V as channel volume and S_b denoting the helical barrel surface area bounding the channel. Finally, the representative shear rate for channel flow is defined as volumetrically averaged magnitude of the rate-of-deformation tensor:

$$\dot{\gamma}_{\text{rep}} := \frac{1}{V}\iiint \sqrt{2\,\boldsymbol{D}\!:\!\boldsymbol{D}}\,\mathrm{d}V. \tag{16}$$

This representative shear rate can be utilized to obtain power-law viscosity parameters from more realistic rheological models, thus extending the application range of the power-law approach to the transitional shear rate regime. This can be accomplished, for instance, by computing the tangent to the viscosity curve in a double-logarithmic scale at that shear rate level [19]. Volumetric averaging was preferred because the shear rates act throughout the fixed volume of the screw channel segment, rather than being transported with the flowing material.

2.3 | Dimensionless Representation

The governing equations for melt conveying are further converted into dimensionless form according to the theory of similarity. Allowing for the independent influencing parameters on the flow to be identified, this intermediate modeling step brings several advantages: First, the effort for data generation is drastically reduced by avoiding redundant simulations that contain essentially the same information. Second, more slender regression models are obtained that accept only a minimum number of input arguments. Finally, the model predictions can be transferred to different production scales such as larger machine sizes or higher line speeds [12].

The scaling procedure follows the general guidelines by Langtangen and Pedersen [29] and the specifications from our previous modeling task [12], taking the simple down-channel shear flow between parallel plates as a reference case. In total, five influencing variables are required to fully characterize the flow conditions:

- the channel depth ratio h/D as measure of channel curvature,
- the screw pitch ratio t/D,
- the aperture angle β,
- the power-law index n,
- and, interchangeably, the dimensionless down-channel pressure gradient

$$\Pi_p = p'\,\frac{h^{n+1}\sin\varphi_b}{6\,K\,\left(v_b\cos\varphi_b\right)^n} \tag{17}$$

or the dimensionless flow rate:

$$\Pi_V = \frac{2\,\dot{V}}{w_b\,h\,v_b\cos\varphi_b}. \tag{18}$$

For investigating the numerical results and building the regression models, the aperture angle was substituted by the aspect ratio of the unwrapped channel

$$\frac{h}{w_b} = \frac{2\,h/D}{\beta}\,\frac{\sqrt{\pi^2 + (t/D)^2}}{t/D}, \tag{19}$$

which is uniquely related to the other geometrical parameters and represents the influence of the screw flights on the melt flow. This allows for an independent analysis of curvature and flight effects on melt conveying and facilitates comparison with existing approximation models.

The dimensionless equivalents for the viscous dissipation rate and representative shear rate are obtained to:

$$\Pi_Q = \frac{\dot{W}_{diss}\, h^n}{K \left(v_b \cos\varphi_b\right)^{n+1} w_b\, Z_b} \tag{20}$$

and

$$\Pi_S = \frac{\dot{\gamma}_{\mathrm{rep}}\, h}{v_b \cos\varphi_b}. \tag{21}$$

2.4 | Parametric Design Study

To define the database for the upcoming regressions, the dimensionless influencing parameters were varied in a wide range that covers diverse screw designs, polymer grades, and process conditions in single-screw extrusion. For an unbiased evaluation of the models, two independent datasets were generated over the same range: (i) a regression dataset for model development, and (ii) a validation dataset for assessing the final models. Table 1 lists the chosen bounds and levels for each parameter and dataset. Compared to the database from our previous study [30], which comprises only single-flighted channels with aperture angles between 300° and 345°, the range for the aperture angle was extended to a lower limit of 15° with a maximum aspect ratio of 1.3. Such narrow aperture angles occur, for instance, at the start of melt channels in barrier screws. Furthermore, the lower limits for the channel depth ratio and the dimensionless down-channel pressure gradient were set to 0.025 and −1.1, respectively, to accommodate strongly overridden flows across tight cross-sections of high-performance screws in grooved-bush extruders. The upper bound of the dimensionless down-channel pressure gradient $\Pi_{p,\max}$ was adapted to the power-law index n according to Table 2 to avoid design points with negative flow rates.

Within the defined parameter ranges, the levels were chosen differently for each dataset (Table 1): The regression data were sampled at fixed, equidistant step sizes for the parameters h/D through n, and sampled randomly within five equidistant bins for Π_p in the positive and negative range. The randomly scattered Π_p values provide the flexibility to create pumping models in both directions (with either Π_p or the dimensionless flow rate Π_V as target variable). With symmetrical placement of the bins, equal emphasis is placed on pressure-generating and pressure-consuming screw zones, both of which are prominent in high-performance extruders. For the validation dataset, random levels were assigned to all influencing parameters within the bins given in Table 1. These random levels are more likely to represent the continuously distributed data input from real-world extrusion problems.

A full evaluation of the parametric study would comprise 13*10*12*9*21*2 = 589,680 design points. Even on high-performance computing clusters, such a massive number of simulations is not affordable, as they would take several years to complete. Aiming for a reasonable balance between information gain and computation time, a fractional factorial sampling scheme was employed (Figure 2) considering

TABLE 2 | Maximum dimensionless down-channel pressure gradient for each power-law index.

n	$\Pi_{p,\max}$
1.0	1.1
0.9	1.0
{0.8, 0.7}	0.8
{0.5, 0.6}	0.7
< 0.5	0.5

TABLE 1 | Ranges and levels of the dimensionless influencing parameters for the regression and for model validation.

Parameter	Dataset	Min. value	Max. value	Step size	No. of levels
h/D	Regression	0.025	0.325	0.025	13
	Validation			Random (4 bins)	
t/D	Regression	0.6	2.4	0.2	10
	Validation			Random (4 bins)	
β	Regression	$\max\{15°; \beta(h/w_b = 1.3)\}$	345°	30°	12
	Validation			Random (4 bins)	
n	Regression	0.2	1.0	0.1	9
	Validation			Random (5 bins)	
Π_p	Regression	−1.1	$\Pi_{p,\max}(n)$	Random (5 bins < 0, 5 bins > 0)	21
	Validation				

Note: Changes with respect to our predecessor models are highlighted in green.

- all 32 corner points with extreme parameter levels,
- all 80 edge-midpoints with the median level for one parameter and extreme levels for the remaining four,
- all 80 face-midpoints with the median levels for two parameters and extreme levels for the remaining three,
- and 3000 randomly sampled interior datapoints

for the regression. Further 1000 random design points were selected for the validation dataset. These sampling criteria ensure complete coverage of the design space with four to five intermediate nodes for each parameter on average. With a total number of 4192 design points, the parametric study could be processed within 4 months on a high-performance computer, using a single node with 64 cores of 2 GHz clock frequency and 512 GB memory.

3 | Numerical Solution

3.1 | Simulation Setup

For each design point in the fractional parametric study, the governing equations were solved numerically by means of the finite-volume method using the commercial software package ANSYS Fluent, release 2023R2 [31]. To accelerate the pre- and post-processing of the simulations, the simulation setup was parametrized and automated within the multi-physics software environment ANSYS Workbench, release 2023R2 [32]. This included the update of geometrical, numerical and physical inputs, the monitoring of the solution process, as well as the evaluation of the target and test variables of interest. As the ANSYS solvers operate only on dimensioned variables, a representative process scale was defined with a barrel diameter of 50 mm, a power-law consistency of 500 Pa s^n, and a relative down-channel barrel velocity of 1 m/s. The screw channel dimensions and operating conditions for each design point were then computed from the five dimensionless influencing parameters and these three scaling variables using Equations (17–19). After completion of the simulations, Equations (17), (18), (20), and (21) were applied to transform the three target variables into their dimensionless equivalents. Detailed information on the configuration of the numerical solution process is given in the following two sub-sections.

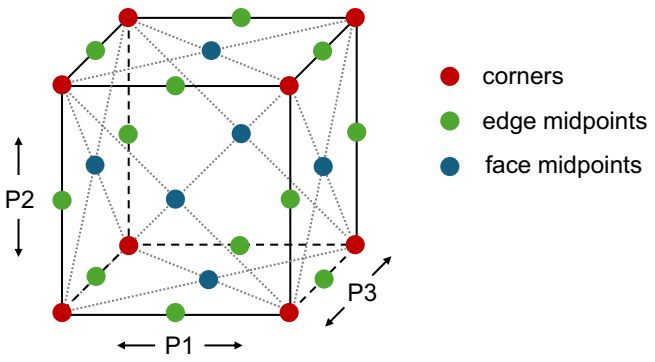

FIGURE 2 | Schematic illustration of the fractional factorial sampling scheme for a three-dimensional design space with input parameters P1–P3. Random inner design points are not shown for clearer visualization. The concept applies analogously to the five-dimensional space in this study.

3.1.1 | Parametric Domain Discretization

Achieving accurate solutions with the finite-volume method requires a computational grid of sufficient fineness and quality. Considering the large variety of channel segments in high-performance screws, ranging from very elongated to boxy shapes, a fixed grid configuration is unlikely to fit for all design points: In general, more divisions are needed along longer dimensions compared to shorter ones to avoid highly stretched cells, which may severely compromise numerical accuracy for the diffusion-dominated flows in polymer extrusion. For this reason, we deployed a parametric domain discretization that adapts to the channel shape under investigation.

Figure 3 illustrates the grid structure for a particular channel segment. In any case, the flow domain was meshed by regular hexahedral cells. To resolve the stronger velocity gradients close to the walls at minimum computational expense, the axial cross-section was further partitioned into two regions: (i) a concentric core with uniform cell size and (ii) a surrounding shell with shrinking cell edges towards the walls. The cell edge lengths along the shell thickness $l_{c,\mathrm{shell}}$ reduce exponentially,

$$l_{c,\mathrm{shell}}{}^{(k+1)} = l_{c,\mathrm{shell}}{}^{(k)}\, BF^{-\frac{1}{N_{d,\mathrm{shell}}}}, \tag{22}$$

with $N_{d,\mathrm{shell}}$ as the number of shell layer divisions and the bias factor BF as ratio between the longest and shortest edge. The cross-sectional grid was expanded into the third dimension using the sweep method with constant cell size in down-channel direction. The three-dimensional grid structure is thus defined by the following numerical parameters:

- the radial and angular spacings of the shell,
- the divisions of the shell in the radial and circumferential directions,
- the bias factors for the shell in the radial and circumferential directions,
- the divisions of the core in the radial and circumferential directions,
- and the number of divisions in down-channel direction.

To account for the different channel shapes of each design point, the grid parameters were formulated as functions of the three main proportions of the screw channel

$$r_{\mathrm{dim,cs}} = \max\left(\frac{h}{\beta\frac{D-h}{2}}; \frac{\beta\frac{D-h}{2}}{h}\right), \tag{23}$$

$$r_{\mathrm{dim,rad}} = \frac{\max\left(h; \beta\frac{D-h}{2}; \sqrt{D^2\pi^2 + t^2}\right)}{h}, \tag{24}$$

$$r_{\mathrm{dim,ang}} = \frac{\max\left(h; \beta\frac{D-h}{2}; \sqrt{D^2\pi^2 + t^2}\right)}{\beta\frac{D-h}{2}}, \tag{25}$$

as well as three numerical parameters that control the grid fineness:

- the ratio of core divisions to shell layer divisions r_{divs},
- a scaling factor for the core divisions α_{core},
- and a growth rate sensitivity β_{GR}.

The functional relationships for grid generation are provided in Supplementary File S2 attached to this article. They were determined heuristically under the prerequisites of:

- a smooth transition between the core and shell layer,
- a maximum cell growth rate of 1.2,
- and less than 100% deviation among the total cell numbers

for all design points, considering the channel shapes with the most extreme and most balanced proportions. These conditions favored quick and stable convergence throughout the entire parametric study.

3.1.2 | Solver Settings

Table 3 lists the settings for the finite-volume solver that computes the target variables for each design point. The continuity and momentum equations were solved in a coupled manner for the velocity and pressure fields, which facilitate convergence compared to segregated approaches. To determine the velocities and pressures at the cell faces, quadratic upwind interpolation (QUICK) and the pressure staggered option (PRESTO) were chosen as the most accurate schemes for regular swept meshes in curved flow domains. The Rhie–Chow distance-based method was preferred for computing fluxes, as this approach generally performs better alongside the parametric domain discretization. Gradients were calculated by the least-squares cell-based method with a standard limiter and an additional correction for warped cell faces. This correction is important because all grid cells are aligned to the curved boundaries of the screw channel.

Four measures were taken to increase solver robustness throughout the entire design space: First, the field variables were reset to zero for each new design point. In addition, the Biconjugate Gradient Stabilization Algorithm (BCGSTAB) was applied on the matrix level, whereas under-relaxation factors of 0.5 were set for all field variables between successive iterations. Lastly, the screw speed and pressure gradient were gradually raised to their final values by a linear ramp function

$$\left[\omega^{(i)}; p'^{(i)}\right] = \left[\omega; p'\right] \min\left(i; 20^{1/n}\right) \tag{26}$$

during the early iterations. The transitional interval was expanded for cases with lower power-law indices, for which convergence is generally more difficult to achieve.

The numerical solution process was monitored by tracking the residuals for the continuity and momentum equations, as well as the evolution of all target variables over the iterations. The simulations were terminated when one of the following criteria was met: (i) all residuals and the standard deviations of all target variables over 60 successive iterations fell below the respective thresholds in Table 3, or (ii) 6000 iterations had passed. For most design points, fewer iterations were sufficient to attain convergence. In the remaining rare cases, converged solutions were obtained by repeating the simulations with a continuity residual threshold of 10^{-9} up to 60,000 iterations. To assess the overall numerical accuracy of the simulations, we further evaluated

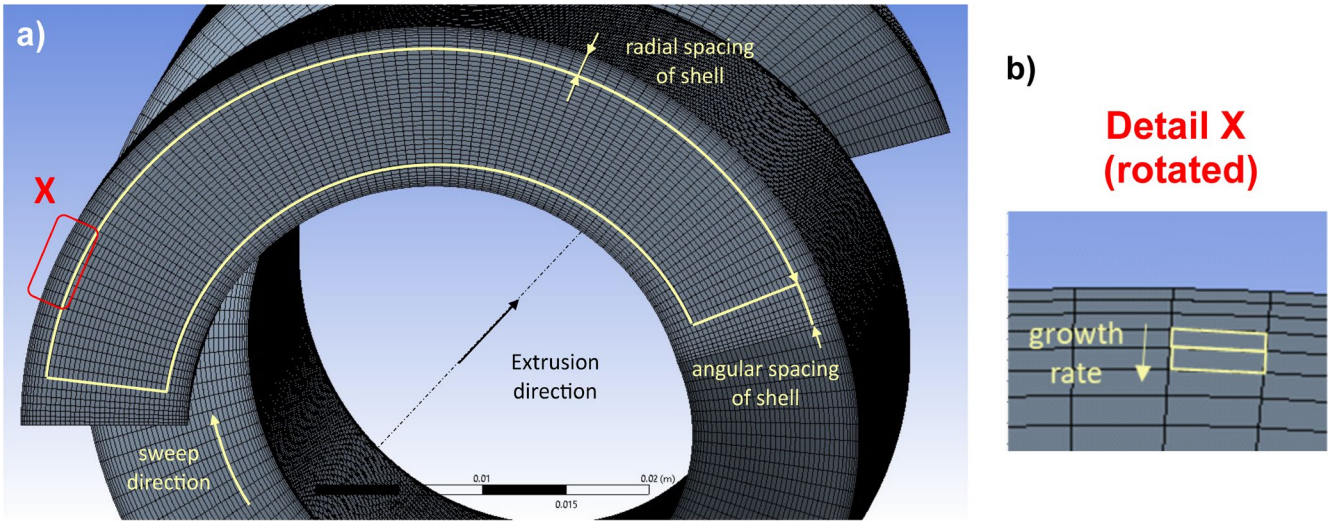

FIGURE 3 | Numerical grid for a screw channel with $h/D = 0.2$, $t/D = 1.4$, and $\beta = 165°$: (a) Overall view showing the cross-sectional and down-channel discretization, (b) enlarged view of the local grid refinement. The yellow lines mark the partition between the core and shell region of the axial cross-section.

TABLE 3 | Settings for the finite-volume solver in ANSYS Fluent.

Solution methods	
Equation system	Coupled
Flux computation	Rhie–Chow distance-based
Velocity interpolation	QUICK
Pressure interpolation	PRESTO
Gradient computation	Least-squares cell-based
Warped-face gradient correction	✓
Gradient limiter	Standard
Solution controls	
Stabilization	BCGSTAB
Flow Courant number	200
Momentum relaxation factor	0.5
Pressure relaxation factor	0.5
Solution monitors	
Continuity residual tolerance	10^{-5}
Momentum residual tolerance	10^{-6}
Target variable tolerance	10^{-3}
Used iterations for evaluation	60
Maximum iterations	6000

the scaled residual of the global power balance on each channel segment

$$r_e = \frac{\dot{W}_{\text{diss}}}{P_{\text{mech}} - \dot{V}\left(p_{\text{out}} - p_{\text{in}}\right)} - 1 \tag{27}$$

that compares the volumetrically evaluated viscous dissipation rate to the value derived from the mechanical drive power and pumping power for extrusion. This accuracy metric is influenced by discretization, truncation, as well as round-off errors.

3.1.3 | Preliminary Investigations

Prior to the execution of the parametric study, a grid refinement study was performed to optimize the grid control parameters for the least expensive grid-independent solution. Since an exhaustive trial across all design points was unaffordable, only four critical cases listed in Table 4 were examined: The first three setups refer to a Newtonian fluid in a slit-like channel, allowing for additional comparison with an analytical solution. The final setup for a strongly shear-thinning fluid in a boxy channel was expected to yield the highest velocity gradients in each direction, which still needed to be sufficiently resolved. For each of these cases, the grid control parameters were varied in the order given in Table 5, with the former parameters kept fixed and the later ones at their coarsest level.

TABLE 4 | Extrusion setups for the grid refinement study.

Parameter	Case 1	Case 2	Case 3	Case 4
h/D	0.025	0.025	0.025	0.025
t/D	2.4	2.4	2.4	0.6
β	345	345	345	15
n	1.0	1.0	1.0	0.2
Π_p	−1.1	0	0.9	−1.1

TABLE 5 | Variation of the grid control parameters (optimum values highlighted in blue).

Parameter	Values
α_{core}	{40, 50, 60, 70}
r_{divs}	{3, 2.5, 2, 1.5}
β_{GR}	{0.04, 0.05, 0.06}

The solution was considered grid-independent once each target variable was affected by less than 1%. The highlighted parameter values struck an optimum balance between discretization error and computation time.

With the simulation setup being finally adjusted, numerically computed dimensionless flow rates and dissipation rates were validated against the exact analytical solutions by Carley et al. [6] and Mohr and Mallouk [7]. For a Newtonian fluid in a slit-like channel, the numerical values match the analytical predictions within an absolute margin of 0.03 or a relative margin of 3% (Figure 4). Considering the small remnant curvature and flight effects even for this extreme setup, the numerical results are in good agreement with theory.

3.2 | Numerical Results

The extended parameter range of the simulations provides new insights into the melt conveying behavior of single-screw extruder channels: With the additional degree of freedom for the channel aspect ratio, the influence of three-dimensional channel curvature can now be examined independently from the screw flights. To highlight the relevance of curvature effects especially for high-performance screw design, exemplary numerical results are presented for a melt channel of an industrial barrier screw. As these channels are typically long and narrow, well-conditioned flow rates and dissipation rates are key to avoid excessive pressures and overheating the polymer inside the extruder.

3.2.1 | Effect of Channel Curvature on Pumping Capability

Figure 5 illustrates the effect of the channel depth ratio h/D on the dimensionless flow rate for a Newtonian polymer melt at various operating points. At a screw pitch ratio t/D of 1.8 (Charts a and b), the dimensionless flow rate consistently drops with stronger

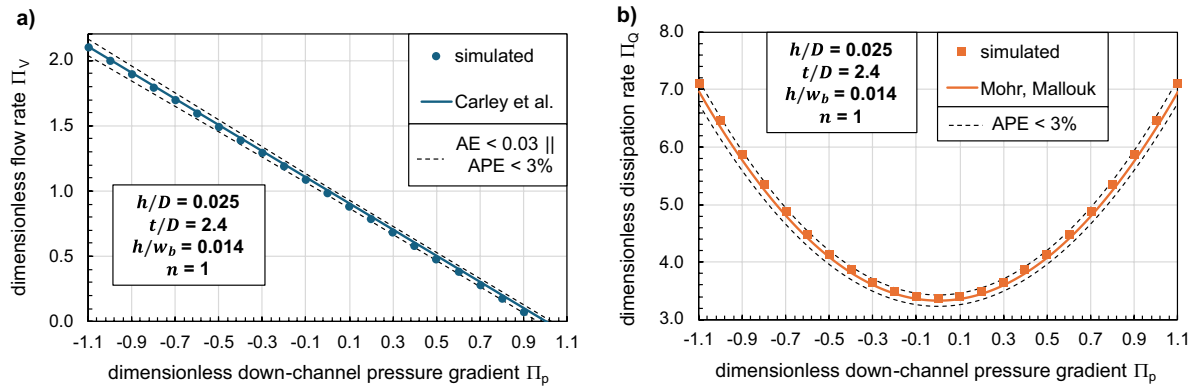

FIGURE 4 | Dimensionless flow rates (a) and dissipation rates (b) of a Newtonian fluid in a slit-like channel, as obtained from the three-dimensional simulations (points) and the respective analytical solutions of Carley et al. and Mohr and Mallouk (solid curves). The thin-dashed lines indicate the margins for an absolute error below 0.03 or an absolute percentage error below 3%.

curvature, and the reduction is similar for all pressure gradients and aspect ratios considered. For channel depth ratios above 0.15, which are frequently found in high-performance screws, the pumping capability is affected by 5%–20%. However, a lower screw pitch ratio of 1.4 (Chart c) partly reverses this trend: Here, the dimensionless flow rate declines less sharply for pressure neutral zones and even slightly increases for overridden zones. These observations can be explained by two competing effects: On one hand, the radial channel taper diminishes the cross-sectional area compared to the unwrapped configuration according to

$$A^* = \frac{A_{\text{curved}}}{A_{\text{unwound}}} = \frac{\pi^2 + (t/D)^2 - \sqrt{\left(\pi^2 + (t/D)^2\right)\left[(1-2\,h/D)^2\,\pi^2 + (t/D)^2\right]}}{2\,\pi^2\,h/D}. \tag{28}$$

The loss of cross-sectional area becomes more significant for higher values of h/D and t/D (Chart d) and hence dominates for large t/D. On the other hand, the area of the laminar flow layer also shrinks radially towards the screw root, which gives rise to higher shear stresses and shear rates in the lower portion of the channel. This results in more convex down-channel velocity profiles and thus counteracts the flow rate reduction due to lost cross-sectional area. The simulation results closely match the analytical solution of Booy [8] except for very large channel depth and aspect ratios. In this regime, Booy's flight correction factors for a constant, average channel width become inaccurate: As the flight flanks diverge towards the barrel, they restrict higher flow velocities to a lesser extent, leading to slightly higher dimensionless flow rates in the fully three-dimensional case.

For a strongly shear-thinning melt, channel curvature affects the dimensionless flow rate differently, as shown in Figure 6 for $t/D = 1.8$ and a power-law index $n = 0.3$: Higher channel depth ratios steadily increase Π_V for pressure-neutral and pressure-consuming zones, and they keep Π_V at a constant level for the pressure-generating operating point. In this case, the effect of local shear stress concentration cancels or even overrules the effect of reduced cross-sectional area, which can be related to the shear-thinning nature of the polymer: The flow rate responds more sensitively to higher shear stresses due to the progressively rising shear rate. The curvature-induced increase is attenuated at higher channel aspect ratios (Chart b), resulting from the stronger flow restriction of the converging flights towards the screw root. The converging flights also explain the flat optimum for overridden zones, for which the flight effect matters most. Compared to conventional metering screws, the larger screw pitch ratios and aspect ratios in high-performance screws dampen the influence of curvature on pumping capability for strongly shear-thinning fluids.

3.2.2 | Effect of Channel Curvature on Viscous Dissipation

Figure 7a,b highlights the impact of the channel depth ratio h/D on the dimensionless average specific dissipation rate for a Newtonian melt. With stronger channel curvature, viscous heating becomes more intense, and the sensitivity to the channel depth ratio is hardly affected by the dimensionless down-channel pressure gradient. The increased specific dissipation in curved channels is largely caused by the radial contraction of the screw channel: As the laminar flow layers shrink and the flight flanks converge, additional shear stress accumulates in the bottom region of the channel. In total, however, the dimensionless dissipation rate rises only up to a critical value of h/D, followed by a decline when the channel depth ratio grows further (Figure 7c,d). The reversing trend results from the smaller melt volume in curved channels compared to the unwrapped configuration. Apparently, the volume reduction compensates for the increased shearing above a certain threshold for channel curvature. As these counteracting effects partly balance each other, the total dissipation is much less influenced by channel curvature than the specific average.

At larger aspect ratios h/w_b, the curvature-induced increase in both specific and total dissipation becomes more pronounced. Furthermore, the peak of the dimensionless total dissipation rate is shifted towards higher h/D values. This phenomenon is linked to the narrowing channel width in radial direction, as the locally higher shear rates close to the screw flights cover a larger portion of the channel. In narrow channels of high-performance screws, even moderate channel depth ratios ($h/D = 0.1$) already

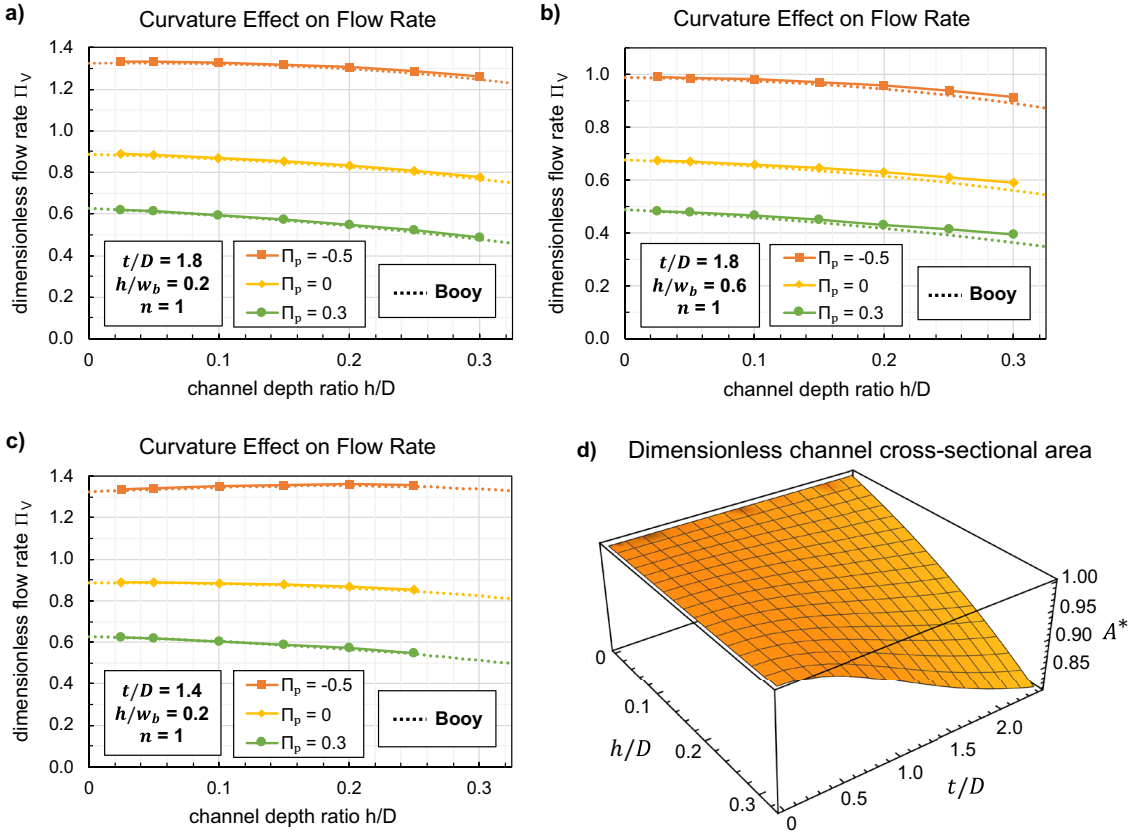

FIGURE 5 | (a–c) Variation of the dimensionless flow rate with the channel depth ratio h/D for a Newtonian polymer ($n = 1$) at typical operating conditions in barrier screws. The dotted lines indicate the analytical approximation proposed by Booy. (d) 3D plot of the dimensionless channel cross-sectional area A^* as a function of the channel depth ratio h/D and screw pitch ratio t/D.

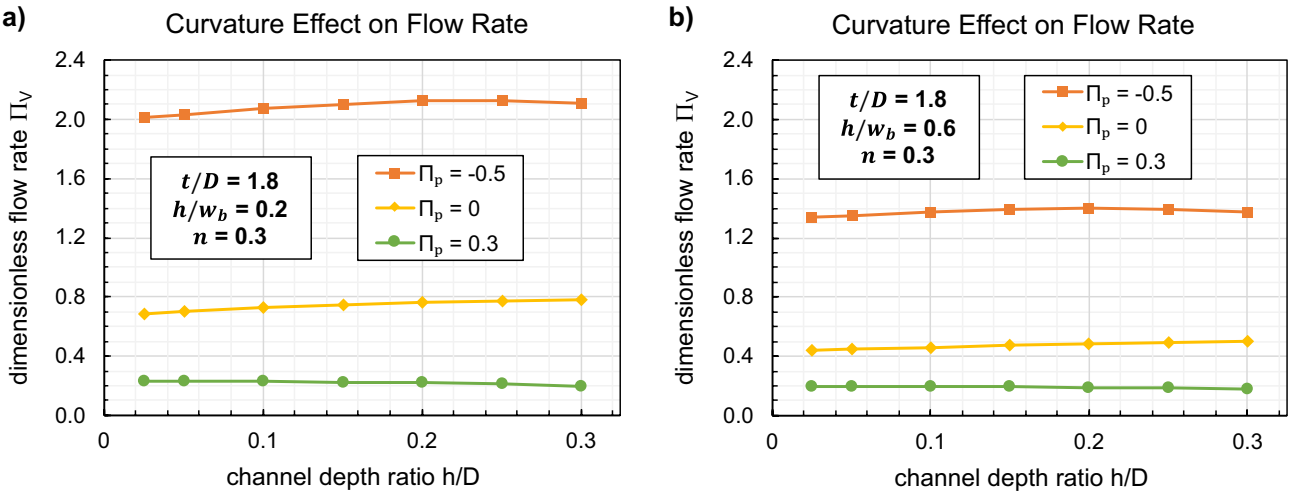

FIGURE 6 | Variation of the dimensionless flow rate with the channel depth ratio h/D for a strongly shear-thinning polymer ($n = 0.3$) at typical operating points in barrier screws: (a) channel aspect ratio $h/w_b = 0.2$ and (b) channel aspect ratio $h/w_b = 0.6$.

affect the total dissipation rate for Newtonian melts by more than 5% (Figure 7d).

The characteristics change again if a strongly shear-thinning melt is processed. According to Figure 8a,b, the average dimensionless specific dissipation rate still rises with larger channel depth ratios h/D, but the sensitivity to curvature is lower compared to the Newtonian case. Moreover, curvature becomes distinctly more influential at higher magnitudes for the dimensionless down-channel pressure gradient. Both observations are a direct consequence of the shear-thinning behavior, which softens the increase in viscous dissipation and reduces flow

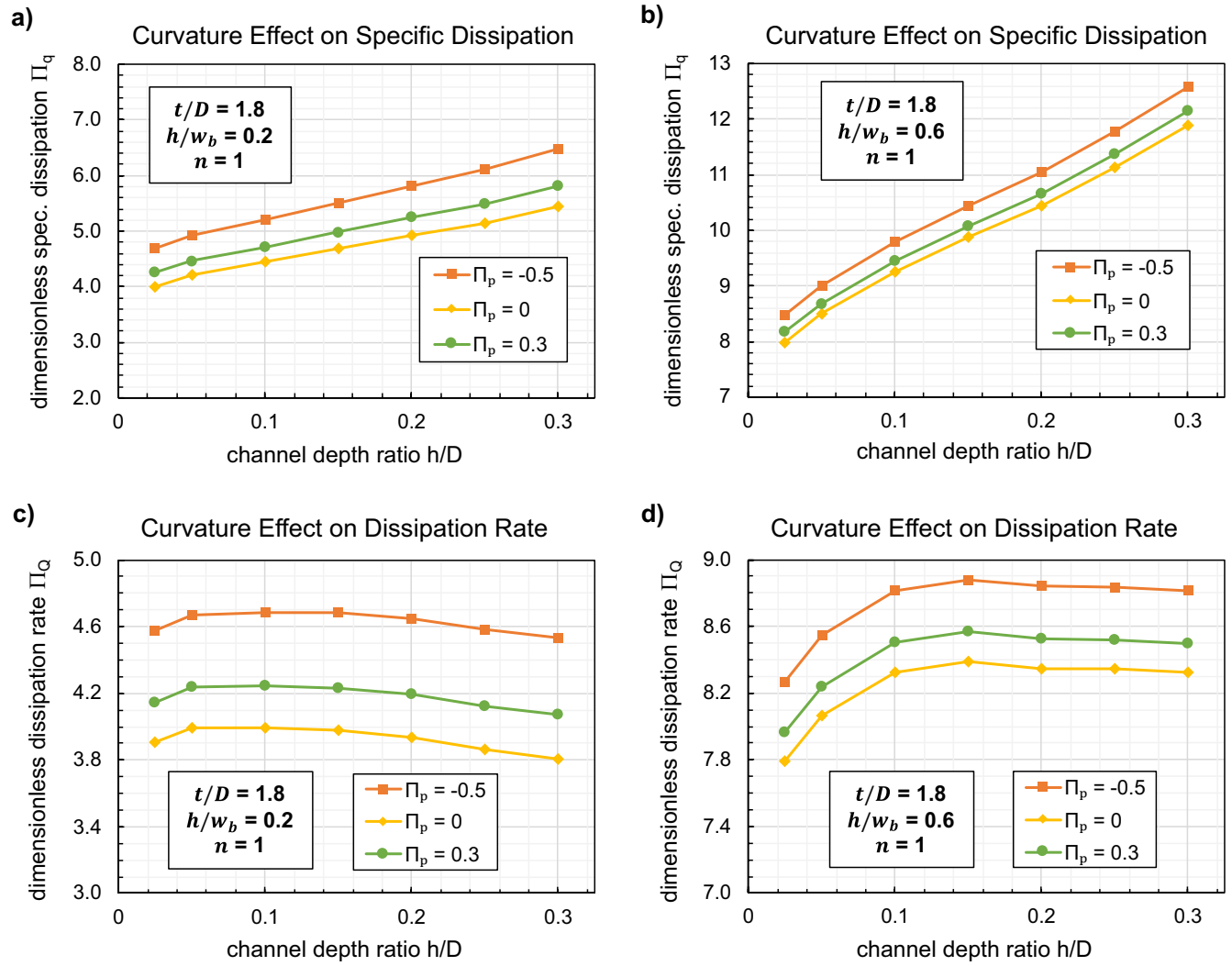

FIGURE 7 | Variation of the dimensionless average specific dissipation rate (a, b) and the dimensionless total dissipation rate (c, d) with the channel depth ratio h/D for a Newtonian polymer ($n = 1$) at typical operating points in barrier screws.

resistance at higher shear rates. The total dimensionless viscous dissipation rate, as shown in Figure 8c,d, drops continuously with stronger channel curvature. Due to the milder increase in specific dissipation, the impact of the lost flow channel volume significantly outweighs the contribution of locally increased shear rates. In wide channels of high-performance screws with h/D greater than 0.1, curvature reduces total dissipation by 10%–20% for strongly shear-thinning melts.

Larger aspect ratios h/w_b exacerbate the increase in specific dissipation due to curvature (Chart b), thus limiting the decline in total dissipation (Chart d), but only for pressure-neutral and throttled zones. For a strongly overridden zone ($\Pi_p = -0.5$), in contrast, the interaction between curvature and screw flights on viscous dissipation almost vanishes: Higher lateral shear rates exerted by the converging flights are balanced by lower radial shear rates due to a more restricted flow. The overall curvature effect on total dissipation is in a lower range for narrow channels, but it still exceeds 5% for $h/D > 0.1$.

4 | Analytical Approximation

After completion of the parametric study, the dimensionless local melt conveying characteristics are merely given as a finite list of discrete parameter values. Actual parameter combinations in single-screw extrusion, however, will generally deviate from those particular cases. To evaluate further design points without re-running time-consuming numerical simulations, the numerical results were approximated by analytical regression models. In total, three continuous functional expressions were derived that predict

- the dimensionless flow rate for a given pressure gradient

$$\Pi_V\left(h/D,\ t/D,\ h/w_b,\ n,\ \Pi_p\right),$$

- the dimensionless dissipation rate for a given flow rate

$$\Pi_Q\left(h/D,\ t/D,\ h/w_b,\ n,\ \Pi_V\right),$$

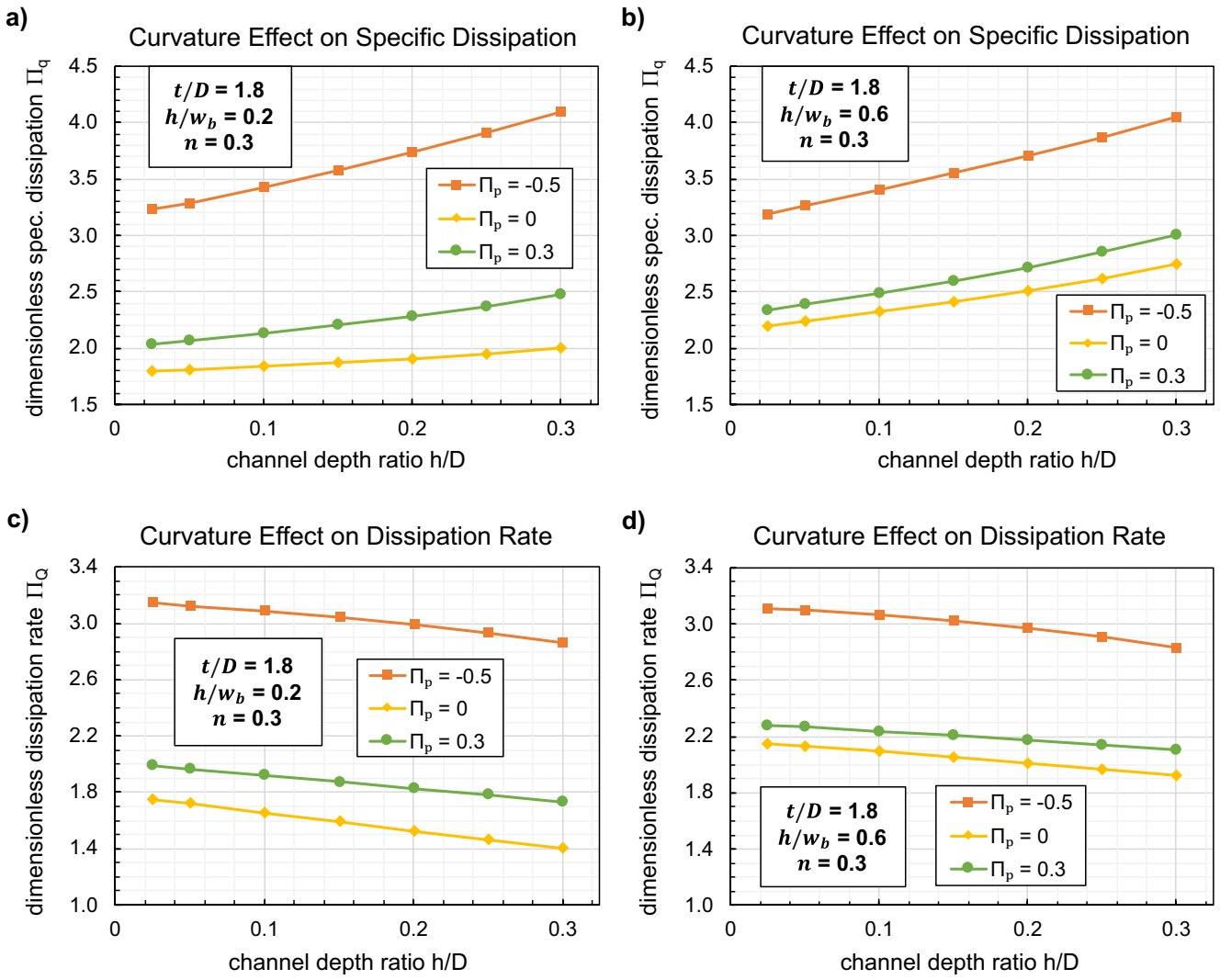

FIGURE 8 | Variation of the dimensionless average specific dissipation rate (a, b) and dimensionless total dissipation rate (c, d) with the channel depth ratio h/D for a strongly shear-thinning polymer ($n = 0.3$) at typical operating points in barrier screws.

- and the dimensionless average shear rate for a given flow rate

$$\Pi_S\left(h/D,\ t/D,\ h/w_b,\ n,\ \Pi_V\right)$$

throughout the entire design space.

The development of these model equations was accomplished by symbolic regression. Rather than fitting model coefficients of a presumed function type, symbolic regression infers hidden functional dependencies from the numerical data, thus optimizing model structure and coefficients simultaneously. By this means, complex nonlinear and coupled effects can be captured, which especially occur with shear-thinning melts flowing through three-dimensional curved channels (see Section 3.2). Given the vast pool of suitable mathematical expressions, the search for an optimum model was driven by genetic programming—a heuristic optimization technique inspired by natural evolution: Starting from a random population of simple models, the individual models were randomly recombined, modified, and partially replaced by next-generation candidates of superior fitness to the numerical dataset. This procedure was continued over multiple generations until a satisfactory model quality was reached. Detailed information on genetic algorithms is given by Affenzeller et al. [33]. The use of symbolic regression with genetic programming has already proven successful for various polymer processing problems [17, 34–37], including our preceding study on a similar modeling task. Thus, we preferred this data-based modeling strategy also for this new series of melt conveying models.

4.1 | Data Preprocessing

The quality and distribution of the numerical samples highly affects the achievable performance of the regression models. For this reason, the numerical data were configured for the upcoming regression in three successive steps: (i) data partition, (ii) data filtering, and (iii) data transformation. First, the regression dataset was split into two subsets—a training set

to develop the models, and a test set to compare models from different runs. The latter is required due to the random operations within the genetic algorithm, which lead to models of variable structure and accuracy even at the same settings. All peripheral and the first 2000 interior design points were considered for training, with the remaining 1000 design points being reserved for testing. Further 1000 independent validation samples have been already defined within the parametric study (Section 2.4) for assessing the final models. Next, each subset was cleared from outliers that corresponded to faulty simulations or practically irrelevant design points. These included cases with either negative flow rates ($\Pi_V < 0$), channel aspect ratios $h/w_b > 1.3$, or global power balance residuals $r_e > 2\%$. After the partition and filtering steps, the numerical database comprised 2119 training samples, 959 test samples, and 862 validation samples. This modified database is now representative for the design space in single-screw extrusion in each subset, with the major information being utilized for model development.

As the last action prior to the regression, the training and test samples were mathematically transformed to attain a more balanced value distribution of the target variables. Scatter plots of these samples, which are provided as Supplementary File S3, reveal a highly uneven spread of the original target values across the design space: Although most design points are scattered within +/−100% around the median, a small proportion of samples exceeds the median by roughly one decade. This discrepancy poses a difficult challenge for symbolic regression, as these exceptional values are overly weighted in the fitness measure, which sacrifices accuracy for the main proportion of use cases. Previous investigations have revealed that the high target levels correspond to strongly overridden screw segments and strongly shear-thinning melts, for which the down-channel pressure gradient dominates the flow [17, 38]. To capitalize on this domain knowledge, each target variable was scaled to

$$\Pi_{V,\mathrm{rel}} = \frac{\Pi_V + 1}{\Pi_{V,\mathrm{app}} + 1}; \tag{29}$$

$$\Pi_{Q,\mathrm{rel}} = \frac{\Pi_Q}{\Pi_{Q,\mathrm{app}}}; \tag{30}$$

$$\Pi_{S,\mathrm{rel}} = \frac{\Pi_S}{\Pi_{Q,\mathrm{app}}^{\,1/(n+1)}}; \tag{31}$$

using theoretical approximation equations $\Pi_{V,\mathrm{app}}$ and $\Pi_{Q,\mathrm{app}}$ by Marschik et al. [17] for superimposed drag and pressure flow through rectangular ducts:

$$\Pi_{V,\mathrm{app}} = f_d - f_p \,\mathrm{sign}(\Pi_p) \frac{3^{\frac{1}{n}}\, n}{2n+1} \left|\Pi_p\right|^{\frac{1}{n}}; \tag{32}$$

$$\Pi_{Q,\mathrm{app}} = f_{d,\mathrm{diss}} + f_p \frac{(2n+1)^n}{n^n} \left|\frac{\Pi_V - f_d}{f_p}\right|^{n+1}. \tag{33}$$

The subfunctions f_d, $f_{d,\mathrm{diss}}$ and f_p, which incorporate the influence of the side walls on each portion of the flow, are given by the expressions

$$f_d = 1 - \frac{a_0 \frac{h}{w_b}\left(a_1 + \frac{h}{w_b} + a_2\, n\right)}{a_3 + a_4 \frac{h}{w_b} + \left(\frac{h}{w_b}\right)^2 + a_5\, n + a_6 \frac{h}{w_b} n}, \tag{34}$$

$$f_{d,\mathrm{diss}} = 1 + \frac{b_0 \left(\frac{h}{w_b}\right)^2 \left(b_1 + \frac{h}{w_b} + b_2\, n\right)(b_3 + n)}{\left(\frac{h}{w_b} + b_4\, n\right)(b_5 + n)}, \tag{35}$$

$$f_p = 1 + \frac{c_0 \frac{h}{w_b}}{1 + c_1 \frac{h}{w_b} + c_2\, n + c_3 \frac{1 + c_4 \frac{h}{w_b} + c_5\, n}{1 + c_6 \frac{h}{w_b} + \frac{c_7}{n} + c_8\, n}}, \tag{36}$$

as disclosed by Marschik and Roland in [39]. For brevity, the coefficients are listed in Supplementary File S4. The transformed target variables $\Pi_{V,\mathrm{rel}}$, $\Pi_{Q,\mathrm{rel}}$, and $\Pi_{S,\mathrm{rel}}$ correct the approximation equations for the additional influences of transverse flow, flow coupling, and curvature. As seen in Charts d-f of Figure S1 in the supplementary file S3, the values of these correction factors are now scattered more evenly within a significantly narrower range. Scaling with theoretical approximations was preferred over simple mathematical transformations due to the domain-specific knowledge introduced into the regression procedure. This approach has been proven most effective to guide the heuristic algorithm towards robust, generally valid models [40].

4.2 | Heuristic Model Derivation

The preprocessed training and test samples were subsequently fed to the open-source software environment Heuristic Lab [41], version 3.3.19, for the symbolic regression. As in our previous study, an Offspring Selection Genetic Algorithm (OSGA) was chosen that optimizes the models solely for prediction quality. Within this algorithm, the symbolic expressions are encoded in parse tree format (Figure 9) indicating the level and order of mathematical operations, and the elementary symbols and their arrangement within the tree are evolved heuristically. As this algorithm tends to create unnecessarily complex models, several constraints were placed on the expression tree structure: First, the expression tree lengths and depths were restricted to maximum values of 100 and 25, respectively. Second, the mathematical building blocks were limited to the function set listed in Table 6, which is likely to represent steady-state characteristic curves in single-screw extrusion. In particular, real-valued power functions were considered instead of trigonometric expressions to reflect the power-law relationship for polymer melt

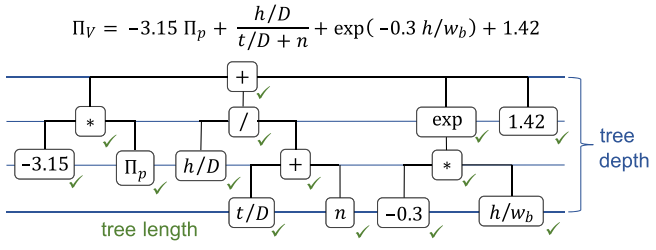

FIGURE 9 | Exemplary symbolic expression tree (adopted from [40]).

TABLE 6 | Settings for the symbolic regression.

Complexity constraints	
Constants	All real numbers
Variables	All independent parameters
Arithmetic operations	+, *, /
Special functions without nesting	Power, exp, log
Maximum tree length	100
Maximum tree depth	25
Algorithm control parameters	
Initial population size	1000
Crossover	Subtree swapping
Crossover probability	90%
Mutator	Multi-expression-tree-manipulator
Mutation probability	25%
Selection operator	Proportional selector
Max. selected parents	2000
Max. selection pressure	100
Success ratio	1
Elites	1
Constant optimization iterations	10
Max. generations	50

viscosity. Third, only sums and products of constants and variables were accepted as arguments for the transcendental functions, and nested fractions were only allowed up to second order. The settings for the genetic algorithm itself are also provided in Table 6. They have already proven beneficial in preceding modeling efforts for similar use cases and were therefore adopted in this study.

Within the regression algorithm, the offspring models for the successive generations were selected based on their coefficients of determination

$$R^2 = 1 - \frac{\sum_{i=1}^{n} \left(y_{i,\mathrm{sim}} - y_{i,\mathrm{appr}}\right)^2}{\sum_{i=1}^{n} \left(y_{i,\mathrm{sim}} - \bar{y}_{\mathrm{sim}}\right)^2} \tag{37}$$

on the training dataset, followed by an optimization of the model coefficients. As the inherent randomness of the genetic operations occasionally leads to unfortunate results, the complete regression cycle was repeated 15 times for each target variable with identical settings. The resulting raw expression trees were subsequently simplified by replacing redundant nodes with constants, and the coefficients of the updated model structure were again optimized.

Aside from the coefficient of determination R^2, the prediction qualities of the refined models were assessed by

- the mean absolute error

$$\mathrm{MAE} = \frac{1}{N} \sum_{i=1}^{N} \left| y_{i,\mathrm{sim}} - y_{i,\mathrm{appr}} \right|, \tag{38}$$

- the mean absolute percentage error for all sample values above 0.1

$$\mathrm{MAPE} = \frac{\sum_{i=1}^{N} \begin{cases} \dfrac{\left| y_{i,\mathrm{sim}} - y_{i,\mathrm{appr}} \right|}{y_{i,\mathrm{sim}}} & \text{if} \quad y_{i,\mathrm{sim}} > 0.1 \\ 0 & \text{otherwise} \end{cases}}{\sum_{i=1}^{N} \begin{cases} i & \text{if} \quad y_{i,\mathrm{sim}} > 0.1 \\ 0 & \text{otherwise} \end{cases}}, \tag{39}$$

- and a quality rate

$$\mathrm{QR} = \sum_{i=1}^{N} \begin{cases} i & \text{if} \quad \mathrm{AE}_i < 0.06 \parallel \mathrm{APE}_i < 0.06 \\ 0 & \text{otherwise} \end{cases} \tag{40}$$

defined as proportion of samples with absolute error AE < 0.06 or absolute percentage error APE $< 6\%$. In addition, the models were checked for discontinuities and spurious oscillations or peaks that may compromise the numerical stability of global extruder calculations. The best models for each target were defined by (i) the highest quality rate and (ii) mean absolute percentage error of the combined expressions on the test set, provided (iii) a complete absence of discontinuities in the interpolation regime, and (iv) smooth extrapolation to the limiting case of $h/w_b = 0$. The latter criterion is crucial for modeling undercut flights in high-performance screws, which is handled by a weighted average of two- and three-dimensional conveying characteristics [24]. The preferred model terms for the transformed targets were finally mathematically rearranged for better readability and a minimum number of operations.

4.3 | Prediction Models

The symbolic regression analysis finally yielded three analytical equations for the relative dimensionless flow rate $\Pi_{V,\mathrm{rel}}$, the relative dimensionless dissipation rate $\Pi_{Q,\mathrm{rel}}$, and the relative dimensionless average shear rate $\Pi_{S,\mathrm{rel}}$:

$$\Pi_{V,\mathrm{rel}} = \frac{D_1 \left(D_2 + D_3\right)}{D_4 + D_5} + \frac{D_6}{D_7 \left(D_8 + D_9\right)} + D_{10}, \tag{41}$$

$$\Pi_{Q,\mathrm{rel}} = \frac{E_1 E_2 \left(E_3 + E_4\right)}{E_5 \left(E_6 + E_7\right) E_8 + E_9} + e_{55}, \tag{42}$$

$$\Pi_{S,\mathrm{rel}} = F_1 \left(F_2 + F_3\right) \left(F_4 F_5 + \frac{1}{F_6 + F_7 + F_8} + F_9\right) + F_{10} + F_{11}, \tag{43}$$

with subfunctions D_{1-10}, E_{1-9}, and F_{1-11} that contain a total number of 46, 55, and 58 coefficients, respectively. The expressions of these subfunctions and the model coefficients rounded up to six significant digits are provided in Supplementary Files S5–S7. The complete prediction models for the dimensionless local melt conveying characteristics are obtained by inverting the respective transformation Equations (29–31):

$$\Pi_V = \Pi_{V,rel}\left(\Pi_{V,\mathrm{app}} + 1\right) - 1, \tag{44}$$

$$\Pi_Q = \Pi_{Q,rel}\,\Pi_{Q,app}, \tag{45}$$

$$\Pi_S = \Pi_{S,rel}\;\Pi_{Q,app}{}^{\frac{1}{n+1}}. \tag{46}$$

Table 7 presents the quality metrics of the complete prediction models on each individual dataset. All models achieve remarkably high approximation quality with coefficients of determination above 0.99, mean absolute percentage errors below 3.5%, and more than 95% share of close predictions. As the metrics remain similar among all datasets and even tend to improve for the validation partition, there is no indication of overfitting. The slightly superior performance on the validation set relates to a smaller proportion of extreme design points, which the regression algorithm generally finds more difficult to capture.

A detailed impression of the predictive capability of the regression models is given in the scatter plots of Figure 10. Each chart shows the absolute percentage error of the respective model on all samples depending on their pair-wise parameter combinations. The validation samples correspond to the scattered points between the vertical stacks at fixed levels for h/D and n. All in all, the prediction error is almost evenly spread along all parameter axes with a marginal number of outliers. Merely the pumping model poses one exception, which yields exceptionally high relative errors for design points with small dimensionless flow rates. Due to the dimensionless flow rate as target variable, however, this observation is mainly caused by numerical augmentation of the absolute error when divided by values close to zero. Indeed, the absolute errors of the pumping model are below average for an overwhelming majority of these design points, rendering them uncritical for full-scale extruder calculations. The approximations of all three models are particularly precise within the most common operating range in polymer extrusion, as indicated by the red bounding boxes in Figure 10: Here, the absolute percentage errors barely exceed 2%. Again, no sign of overfitting is evident, as the color shades of regression and validation samples are undistinguishable throughout the design space. The scatter plots thus demonstrate a comprehensive and consistently high approximation quality of the regression models.

The excellent predictive capability of the analytical model equations is further underlined in Figure 11, which plots characteristic curves alongside simulation data for a typical shallow and deep-flighted segment of a wave screw and different polymer melts. Besides closely matching the simulation data, the continuous graphs of the regression models largely reflect the expected physical behavior: First, the dimensionless flow rates monotonically drop with rising dimensionless down-channel pressure gradient, following a linear function for a Newtonian fluid that becomes steeper and increasingly nonlinear for more shear-thinning melts. Second, both the dimensionless dissipation and shear rate are minimum at the pure drag flow rate and progressively rise when departing from the minimum. Third, higher shear-thinning decreases the dimensionless dissipation rates as well as their sensitivity to the operating point. The same applies to the dimensionless average shear rates, yet to a smaller extent. Finally, the deep-flighted section exhibits lower dimensionless flow rates accompanied by higher dimensionless shear rates, as caused by the combined effect of channel curvature and screw flights. Still, small artifacts appear for the dissipation and shear rate models close to the minima for a power-law index of 0.2. Optimizing or re-training these regression models on additional numerical samples in this range would even further improve the reliability of the predictions.

TABLE 7 | Approximation qualities of the complete models.

Quality metric	Dataset	Flow rate model	Dissipation model	Shear rate model
Coefficient of determination (R^2)	Training	0.997	0.996	0.999
	Test	0.999	0.998	0.999
	Validation	0.997	0.999	0.998
Mean absolute error (MAE)	Training	0.053	0.169	0.059
	Test	0.031	0.093	0.043
	Validation	0.024	0.063	0.030
Mean absolute percentage error (MAPE)	Training	3.3%	1.9%	1.5%
	Test	3.1%	1.8%	1.4%
	Validation	2.8%	1.5%	1.4%
Quality rate (QR)	Training	97.2%	95.9%	98.3%
	Test	98.1%	97.3%	98.7%
	Validation	98.8%	99.1%	99.2%

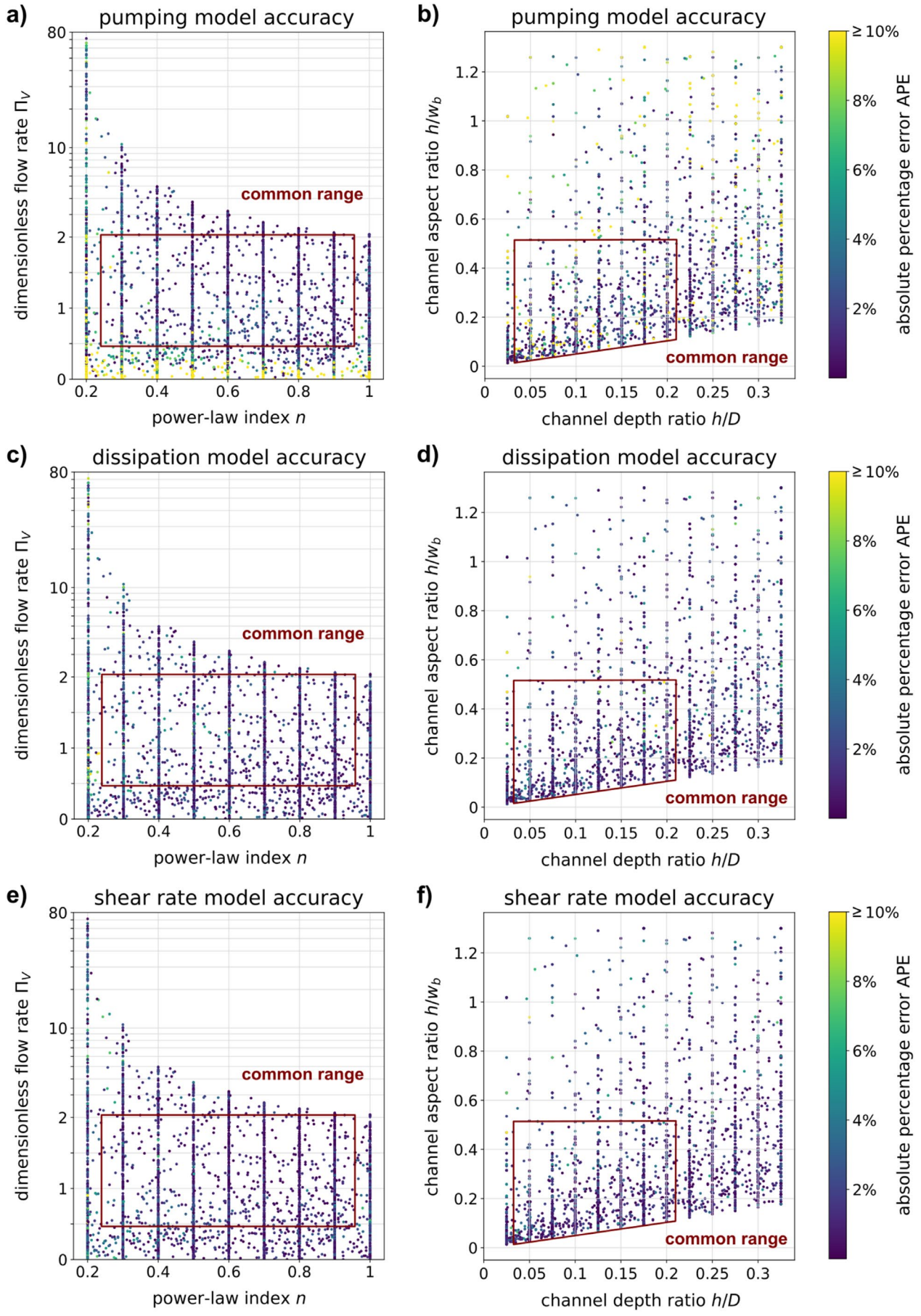

FIGURE 10 | Legend on next page.

FIGURE 10 | Distribution of the absolute percentage errors for the pumping model (Equation 44) (a, b), the dissipation model (Equation 45) (c, d), and the shear rate model (Equation 46) (e, f) across the complete dataset. The red boxes mark the subspace of the most common design points in single-screw extrusion.

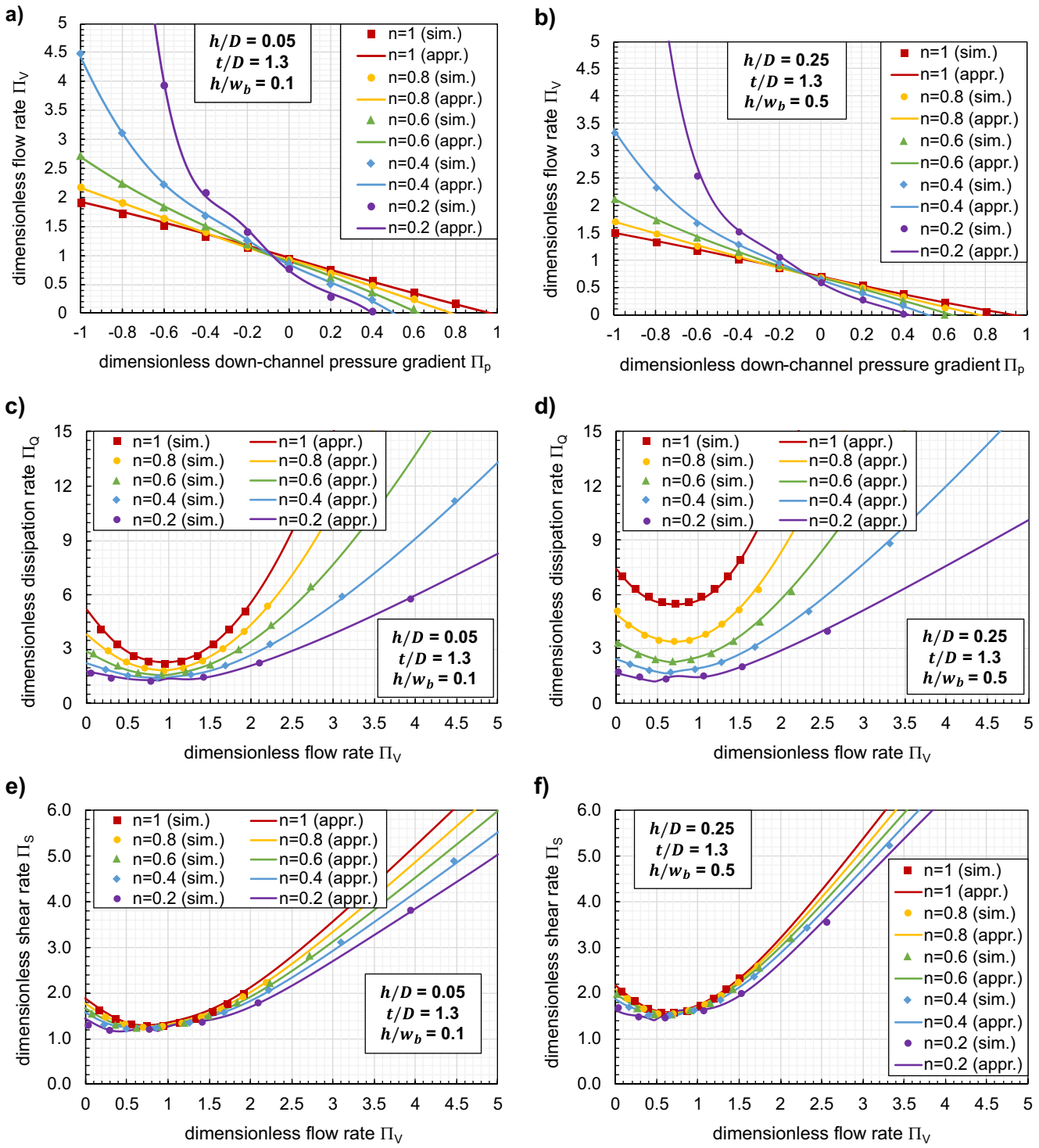

FIGURE 11 | Comparison of simulated (sim.) and analytically approximated (appr.) melt conveying characteristics for typical wave screw segments and various power-law indices: (a, b) dimensionless pumping capability, (c, d) dimensionless dissipation rate, and (e, f) dimensionless average shear rate.

TABLE 8 | Prediction qualities of different analytical channel flow models for single-screw extrusion on the entire dataset.

Quality metric	Channel flow model	Flow rate, Π_V (Π_p)	Dissipation rate, Π_Q (Π_V)	Shear rate, Π_S (Π_V)
Coefficient of determination (R^2)	2D flat, segregated	—	—	0.472
	3D straight	0.811	0.980	—
	3D curved, single-flighted	0.828	0.954	—
	3D curved, generic	0.998	0.996	0.999
Mean absolute error (MAE)	2D flat, segregated	—	—	1.26
	3D straight	0.289	0.521	—
	3D curved, single-flighted	0.341	1.37	—
	3D curved, generic	0.041	0.127	0.049
Mean absolute percentage error (MAPE)	2D flat, segregated	—	—	154%
	3D straight	10.8% ($\Pi_V > 0.1$)	8.4%	—
	3D curved, single-flighted	27.7% ($\Pi_V > 0.1$)	28.2%	—
	3D curved, generic	3.1% ($\Pi_V > 0.1$)	1.8%	1.5%
Quality rate (QR)	2D flat, segregated	—	—	5.9%
	3D straight	63.9%	48.0%	—
	3D curved, single-flighted	71.4%	13.4%	—
	3D curved, generic	97.8%	97.0%	98.6%

To assess the added value of the novel melt conveying models, Table 8 compares their quality metrics on the complete numerical dataset to the scores of three benchmark models: (i) the extended three-dimensional straight channel models by Marschik et al. [17] for the pumping capability and dissipation rate, (ii) the single-flighted, three-dimensional curved channel models by Herzog et al. [12] for the same two relationships, and (iii) a two-dimensional segregated shear rate model

$$\Pi_{S,2D-\mathrm{rep}} = \sqrt{\left[1+3\,e(n)\,\left(\Pi_V - 1\right)\right]^2 + \left[\frac{t/D}{\pi}(1-3\,e(n))\right]^2} \tag{47}$$

based on superimposed drag, pressure and transverse flow in an infinite slit, with the representative radial position

$$e(n) = \begin{cases} \exp(-1/3) & \text{if} \quad n=1, \\ \left(\frac{3\,n}{2\,n+1}\right)^{\frac{n}{1-n}} & \text{otherwise} \end{cases} \tag{48}$$

according to Giesekus et al. [42]. Generally speaking, none of the benchmark models correctly maps the melt conveying characteristics throughout the entire design space: The straight channel equations predict less than 2/3 of flow rates and less than 1/2 of dissipation rates considered at acceptable accuracy, with mean absolute percentage errors around 10%. This moderate but consistent and significant deviation is largely caused by the neglected channel curvature. The single-flighted curved channel models have a slightly better success ratio for the flow rate at the expense of a dramatically worse success ratio for the dissipation rate, accompanied by mean absolute percentage errors exceeding 25%. This indicates a large number of model failures when extrapolating to narrow opening angles—cases that were missing in the training data for deriving these models. The two-dimensional segregated shear rate model performs particularly poorly with a mean absolute percentage error above 100% and a quality rate below 10%. This is not surprising, as the effects of curvature, screw flights, and flow coupling are ignored altogether in this approach. The novel regression models, in contrast, align to the simulation results in more than 97% of all cases, and the mean relative deviations are multiple times lower. Applying heuristic algorithms on a comprehensive database for three-dimensional curved channel flow in multi-flighted screws thus proved as gamechanger to strengthen the validity of the developed equations.

4.4 | Application to Single-Screw Extruders

Despite the high degree of sophistication, the standalone regression models strictly apply only to short, isolated channel segments of constant dimensions. However, various extruder screws in industrial use, in particular high-performance designs, exhibit tapering channel cross-sections along the screw axis as well as undercut flights to promote cross-channel flow. In long metering zones, viscous dissipation further causes a significant melt temperature increase that affects the conveying behavior through temperature-dependent material properties. To accommodate variable flow conditions in the down-channel

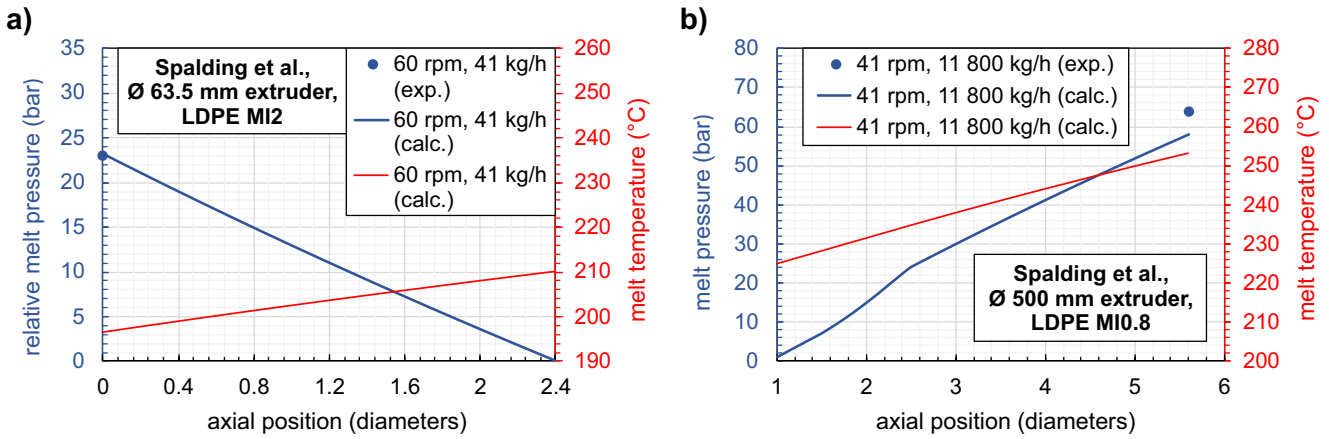

FIGURE 12 | Reported pressure measurements by Spalding et al. (blue dots) compared to calculated axial pressure profiles (blue lines) and axial temperature profiles (red lines) using the novel melt conveying models within non-isothermal network theory: (a) Setup 1 and (b) Setup 2.

direction alongside leakage flow, the melt conveying characteristics need to be implemented in a segmented extruder calculation. Such calculation routines divide each screw channel and flight clearance into short segments where constant flow conditions can be assumed. This approach is now anchored into numerous software packages for single-screw extrusion [43–45]. One promising solution strategy applies the principles of network theory as disclosed in [24, 46]: The average pressures, average temperatures and flow rates along the screw are determined by (i) connecting adjacent screw segments in the down-channel and cross-channel directions and (ii) balancing the mass and enthalpy flows at each connecting node. The hydraulic and thermal characteristics of each segment along the channel could then be obtained from the surrogate models in dimensional form, employing the shear rate model in an inner iteration loop for computing the local power-law viscosity parameters. The mechanical drive power consumed in the metering zone is given by the total dissipation rate and pumping power across all segments:

$$P_{\mathrm{mech}} = \sum_{\mathrm{seg}} \left(\dot{W}_{\mathrm{diss,seg}} + \frac{\dot{m}_{\mathrm{seg}}}{\rho\left(\overline{p}_{\mathrm{seg}}, \overline{T}_{\mathrm{seg}}\right)} \Delta p_{\mathrm{seg}} \right), \tag{49}$$

with $\overline{p}_{\mathrm{seg}}, \overline{T}_{\mathrm{seg}}$ and Δp_{seg} as average pressure, average temperature, and pressure difference across a segment. The reduced influence of undercut flights on the channel flow, as observed in barrier or wave screws, can be considered by a weighted average between the case of finite and zero aspect ratio for all three melt conveying models:

$$\begin{bmatrix} \Pi_{V,\mathrm{eff}} \\ \Pi_{Q,\mathrm{eff}} \\ \Pi_{S,\mathrm{eff}} \end{bmatrix} = \left(1 - \frac{\delta_a + \delta_p}{2\,h}\right) \begin{bmatrix} \Pi_V \\ \Pi_Q \\ \Pi_S \end{bmatrix} + \frac{\delta_a + \delta_p}{2\,h} \begin{bmatrix} \Pi_V \\ \Pi_Q \\ \Pi_S \end{bmatrix}\Bigg|_{\frac{h}{w_b}=0}, \tag{50}$$

with δ_a and δ_p representing the respective clearances at the active and passive flight flank. This framework can evaluate extrusion processes within a few minutes even for long and complex screws, rendering it an attractive option for extensive design studies.

The ability of the new surrogate models to predict real-world extruder performance is demonstrated by recalculating two extrusion experiments reported by Spalding et al. [47]: The first setup refers to a constant-shaped, single-flighted metering zone of a 63.5 mm diameter extruder, while the second one involves a double-flighted three-zone screw of a 500 mm diameter extruder. For additional consideration of leakage flow and thermal effects, the models were applied alongside non-isothermal network analysis as disclosed by Roland et al. [46], using the equations of Marschik et al. [48] to determine the element properties across the flight clearances. The solver settings for the calculations are documented in Supplementary File S8. As illustrated in Figure 12, the calculations almost perfectly match the measured pressure of Setup 1, whereas the pressure recording of Setup 2 is predicted within an error margin of 10%. The latter deviation can still be regarded as acceptable, as the overall uncertainties related to the experimental setup and the process are in a similar range. The calculations further provide reasonable melt temperature values, showing the expected degressive rise in the axial direction. Considering the vastly different production scales between these two cases, the results thus confirm the excellent scalability of the dimensionless melt conveying characteristics. A broader experimental model validation that also encompasses wave-dispersion screws will be addressed in an upcoming publication.

Based on cases of pure melt flow in a rotating frame of reference, the regression models primarily address melt conveying zones in extrusion mode. Most single-screw plasticating units, however, are fed with solid-state material that is converted into melt while transported. At the later stage of melting or for wave-type melting zones, the melt-dominated approach still works surprisingly well, as demonstrated in a previous validation study [24]. Due to the dispersion of the solids into small particles that are surrounded by melt and are also softening quickly, material transport remains largely governed by viscous forces in these cases. Yet in the earlier stages of the phase transition zone, where solid and molten polymer move side by side, the flow in the melt pool becomes influenced by the radial and down-channel velocities of the solid bed. Accurate melt conveying characteristics for this region thus require an extended flow simulation database

that incorporates the dimensionless form of these velocity components as further influencing parameters. For modeling the conveying of solids in the feeding section, different numerical approaches, such as the discrete element method, need to be consulted. A further extension of the models is required for injection molding: The axial retraction speed of the screw considerably alters the flow pattern and thus needs to be considered as an additional influencing parameter in dimensionless form. Developing further generalized models for these use cases is suggested as an objective for future research.

5 | Conclusion

This work features the most universally applicable regression models to date worldwide for predicting the local melt flow rates, viscous dissipation rates, and average shear rates in metering channels of single-screw extruders. Based on a computational parametric study related to flow of power-law fluids in confined channel segments, these models provide dimensionless analytical equations depending on five independent variables: (i) the channel depth ratio h/D, (ii) the screw pitch ratio t/D, (iii) the channel aspect ratio h/w_b, (iv) the power-law index n, and (v) the dimensionless down-channel pressure gradient Π_p or dimensionless flow rate Π_V depending on the target. The models combine two key features that set them apart from previous analytical approaches: First, they fully capture the influence of three-dimensional channel curvature alongside the shear thinning behavior of polymer melts. As revealed in the parametric study, curvature may affect the pumping and dissipation characteristics by more than 10%. Second, the models precisely and continuously map a comprehensive design space that covers both conventional and high-performance extrusion conditions—including deep and narrow channel sections of multi-flighted screws ($h/D \leq 0.325$; $h/w_b \leq 1.3$), as well as strongly overridden zones in high-speed machines ($\Pi_p \geq -1.1$). Throughout this wide-ranging design space, the new characteristic equations impress with outstanding prediction quality: On independent simulation data, they achieve mean absolute percentage errors below 3.5%, which by far excels the capabilities of existing approximation models. Moreover, they reliably match real-world extrusion data at different production scales when applied alongside non-isothermal network theory. Subsequent analytical corrections additionally allow for mapping undercut flights in barrier and wave screws. Due to their extended scope of validity, the advanced melt conveying models can significantly enhance the accuracy of fast-computing segmented extruder calculations. The improved predictions facilitate screw design and process troubleshooting for a considerably larger variety of melt conveying zones in single-screw extrusion without resorting to time-consuming detailed numerical investigations.

Nomenclature

A channel cross-sectional area

A^* dimensionless channel cross-sectional area

B_a covered cross-sectional area by the active flight flank radius

B_p covered cross-sectional area by the passive flight flank radius

BF cell bias factor

D inner barrel diameter

$\boldsymbol{D}$ rate of deformation tensor

e representative channel position

h channel depth

h/D channel depth ratio

h/w_b channel aspect ratio

K power-law consistency

$l_{c,\mathrm{shell}}$ cell edge length in the shell layer

MAE mean absolute error

MAPE mean absolute percentage error

$N_{d,\mathrm{shell}}$ number of divisions in the shell layer

n power-law index

p melt pressure

p' average axial pressure gradient

P_{mech} mechanical drive power

QR quality rate

r radial distance

$r_{\mathrm{dim,cs}}$ cross-sectional proportion of the flow domain

$r_{\mathrm{dim,rad}}$ radial proportion of the flow domain

$r_{\mathrm{dim,ang}}$ angular proportion of the flow domain

r_{divs} ratio of cell divisions between the shell and core layer

R^2 coefficient of determination

t screw pitch

t/D screw pitch ratio

V channel segment volume

$\boldsymbol{v}$ flow velocity

$\dot{V}$ volumetric flow rate

w channel width

$\dot{W}_{diss}$ viscous dissipation rate

y arbitrary target variable

Z down-channel length per revolution

α_{core} scaling factor for the divisions of the core layer

β aperture angle on the circumference

β_{GR} sensitivity parameter for the cell growth rate

$\dot{\gamma}$ shear rate

$\dot{\gamma}_{rep}$ representative shear rate (volumetric average)

δ_a radial clearance at the active flight

δ_p radial clearance at the passive flight

η melt viscosity

Π_p dimensionless down-channel pressure gradient

Π_Q dimensionless dissipation rate

$\Pi_{Q,\mathrm{app}}$ dimensionless apparent dissipation rate

$\Pi_{Q,\mathrm{rel}}$ dimensionless relative dissipation rate

Π_S dimensionless average shear rate

$\Pi_{S,\mathrm{rel}}$ dimensionless relative shear rate

$\Pi_{V,\mathrm{app}}$ dimensionless apparent flow rate

Π_V dimensionless flow rate

$\Pi_{V,\mathrm{rel}}$ dimensionless relative flow rate

$\boldsymbol{\tau}$ viscous stress tensor

φ pitch angle

ω screw speed

Author Contributions

Daniel Herzog: writing – review and editing, writing – original draft, investigation, validation, methodology, formal analysis, data curation, conceptualization, visualization, software. **Wolfgang Roland:** writing – review and editing, supervision, conceptualization, methodology, project administration, funding acquisition, software. **Christian Marschik:** writing – review and editing, methodology. **Gerald Berger-Weber:** writing – review and editing, supervision, funding acquisition, resources.

Acknowledgments

This work was funded in part by the Austrian Science Fund (FWF, grant-DOI: https://doi.org/10.55776/I4872). Christian Marschik further acknowledges financial support from the COMET Center CHASE, which is funded by the Austrian Research Promotion Agency (FFG). The numerical results of the parametric study were in part achieved using the Austrian Scientific Computing (ASC) infrastructure. Special credits go to Dr. Michael Krieger from the Institute of Fluid Mechanics and Heat Transfer (Linz, Austria) for his consultations on the numerical solution strategy and for providing additional computational resources for the simulations. Moreover, we again express our gratitude to the team of the Institute of Polymer Product Engineering (Linz, Austria), for granting access to three powerful workstations for the symbolic regression. For open access purposes, the author has applied a CC BY public copyright license to any author-accepted manuscript version arising from this submission. Open Access funding provided by Johannes Kepler Universitat Linz/KEMÖ.

Data Availability Statement

The main results generated in this study have been uploaded to the public repository *Zenodo* and can be accessed by the persistent identifiers stated below. These include the dimensionless simulation results from the parametric study (DOI: https://doi.org/10.5281/zenodo.16833944), the complete expressions of the regression models (DOI: https://doi.org/10.5281/zenodo.16834106), and the axial pressure and temperature profiles from the experimental model validation (DOI: https://doi.org/10.5281/zenodo.17209049), formatted as Excel spreadsheets. Other kinds of data are available on request from the authors.

References

1. C. I. Chung, *Extrusion of Polymers: Theory and Practice*, 3rd ed. (Hanser Publishers, 2019).

2. C. Rauwendaal, *Polymer Extrusion*, 5th ed. (Hanser Publishers, 2014).

3. G. A. Campbell and M. A. Spalding, *Analyzing and Troubleshooting Single-Screw Extruders*, 2nd ed. (Hanser Publishers, 2021).

4. H. S. Rowell and D. Finlayson, "Screw Viscosity Pumps," *Engineering* 114 (1922): 606–607.

5. H. S. Rowell and D. Finlayson, "Screw Viscosity Pumps," *Engineering* 126 (1928): 249–250, 385-387.

6. J. F. Carley, R. S. Mallouk, and J. M. McKelvey, "Simplified Flow Theory for Screw Extruders," *Industrial and Engineering Chemistry* 45, no. 5 (1953): 974–978, https://doi.org/10.1021/ie50521a032.

7. W. D. Mohr and R. S. Mallouk, "Flow, Power Requirement, and Pressure Distribution of Fluid in a Screw Extruder," *Industrial and Engineering Chemistry* 51, no. 6 (1959): 765–770, https://doi.org/10.1021/ie50594a034.

8. M. L. Booy, "Influence of Channel Curvature on Flow, Pressure Distribution, and Power Requirements of Screw Pumps and Melt Extruders," *Polymer Engineering and Science* 3, no. 3 (1963): 176–185, https://doi.org/10.1002/pen.760030305.

9. H. J. Zamodits and J. R. A. Pearson, "Flow of Polymer Melts in Extruders. Part I. The Effect of Transverse Flow and of a Superposed Steady Temperature Profile," *Transactions of The Society of Rheology* 13, no. 3 (1969): 357–385, https://doi.org/10.1122/1.549136.

10. W. Roland, C. Marschik, B. Löw-Baselli, and J. Miethlinger, "The Effect of Channel Curvature on the Flow Rate and Dissipation of Power Law Fluids," *SPE ANTEC Tech. Papers* 64 (2018): 3087–3093.

11. K. H. Lim, W. R. Hwang, and S. J. Kim, "A Finite-Element Technique for Flows in the Single Screw Extruder Using a Partial Periodic Unit," *Korea-Australia Rheology Journal* 31, no. 1 (2019): 59–67, https://doi.org/10.1007/s13367-019-0007-4.

12. D. Herzog, W. Roland, C. Marschik, and G. R. Berger-Weber, "Generalized Predictions of the Pumping Characteristics and Viscous Dissipation of Single-Screw Extruders Including Three-Dimensional Curvature Effects," *Polymer Engineering and Science* 64, no. 11 (2024): 5556–5587, https://doi.org/10.1002/pen.26934.

13. H. Potente, "Approximationsgleichungen Für Schmelzeextruder," *Rheologica Acta* 22 (1983): 387–395, https://doi.org/10.1007/BF01333769.

14. H. Potente and C. Obermann, "Screw Drive Power of Single Screw Plasticating Units With Smooth Barrels," *International Polymer Processing* 14, no. 1 (1999): 21–27, https://doi.org/10.3139/217.1523.

15. C. Marschik, W. Roland, B. Löw-Baselli, and J. Miethlinger, "A Heuristic Method for Modeling Three-Dimensional Non-Newtonian Flows of Polymer Melts in Single-Screw Extruders," *Journal of Non-Newtonian Fluid Mechanics* 248 (2017): 27–39, https://doi.org/10.1016/j.jnnfm.2017.08.007.

16. W. Roland, C. Marschik, M. Krieger, B. Löw-Baselli, and J. Miethlinger, "Symbolic Regression Models for Predicting Viscous Dissipation of Three-Dimensional Non-Newtonian Flows in Single-Screw Extruders," *Journal of Non-Newtonian Fluid Mechanics* 268 (2019): 12–29, https://doi.org/10.1016/j.jnnfm.2019.04.006.

17. C. Marschik, W. Roland, and M. Kommenda, "Extended Melt-Conveying Models for Single-Screw Extruders: Integrating Domain Knowledge Into Symbolic Regression," *Polymer Engineering and Science* 63, no. 11 (2023): 3639–3656, https://doi.org/10.1002/pen.26473.

18. C. Marschik and W. Roland, "Predicting the Pumping Capability of Single-Screw Extruders: A Comparison of Two- and Three-Dimensional Modeling Approaches," in *AIP Conference Proceedings*, vol. 2607 (AIP Publishing, 2023), 20002, https://doi.org/10.1063/5.0136774.

19. C. Marschik, W. Roland, and J. Miethlinger, "A Network-Theory-Based Comparative Study of Melt-Conveying Models in Single-Screw Extrusion: A. Isothermal Flow," *Polymers* 10, no. 8 (2018): 929–950, https://doi.org/10.3390/polym10080929.

20. A. Pricci and G. Percoco, "A Generalized Method Aiming at Predicting the Polymer Melt Flow Field in the Metering Zone of Large-Scale Single-Screw Extruders," *International Journal of Advanced Manufacturing Technology* 132 (2024): 277–290, https://doi.org/10.1007/s00170-024-13346-9.

21. W. Roland, M. Kommenda, and G. Berger-Weber, "Application of Symbolic Regression in Polymer Processing," in *24th International Symposium on Symbolic and Numeric Algorithms for Scientific Computing (SYNASC)* (IEEE, 2022), 311–318, https://doi.org/10.1109/SYNASC57785.2022.00056.

22. H. Potente, "Single Screw Extruder Analysis and Design," in *Screw Extrusion: Science and Technology*, ed. J. L. White and H. Potente (Hanser Publishers, 2003), 229.

23. M. A. Spalding, J. Dooley, and K. S. Hyun, "The Effect of Flight Radii Size on the Performance of Single-Screw Extruders," *SPE ANTEC Tech. Papers* 45 (1999): 190–194.

24. C. Marschik, W. Roland, M. Dörner, S. Schaufler, V. Schöppner, and G. Steinbichler, "Application of Network Analysis to Flow Systems With Alternating Wave Channels: Part B. (Superimposed Drag-Pressure Flows in Extrusion)," *Polymers* 12, no. 9 (2020): 1900–1923, https://doi.org/10.3390/polym12091900.

25. W. Ostwald, "Ueber die rechnerische Darstellung des Strukturgebietes der Viskosität," *Kolloid Zeitschrift* 47 (1929): 176–187, https://doi.org/10.1007/BF01496959.

26. A. de Waele, "Viscometry and Plastometry," *Journal of the Oil and Colour Chemists' Association* 6 (1923): 33–69.

27. C. Rauwendaal, T. A. Osswald, G. Tellez, and P. J. Gramann, "Flow Analysis in Screw Extruders-Effect of Kinematic Conditions," *International Polymer Processing* 13, no. 4 (1998): 327–333, https://doi.org/10.3139/217.980327.

28. H. Potente, M. Bornemann, D. Heinrich, and J. Pape, "Influence of Power Law and Isothermal Simplification on the Accuracy in Single Screw Extrusion," *International Polymer Processing* 20, no. 4 (2005): 417–422, https://doi.org/10.1515/ipp-2005-0070.

29. H. P. Langtangen and G. K. Pedersen, "Scaling of Differential Equations," in *Simula Springer Briefs on Computing*, ed. A. Tveito, vol. 2 (Springer International Publishing, 2016), https://doi.org/10.1109/SYNASC57785.2022.00056.

30. D. Herzog, C. Marschik, A. Gugg, and W. Roland, *Simulation Results for Three-Dimensional (Confined) Curved Screw Channels*, version 1 (Zenodo, 2024), https://doi.org/10.5281/zenodo.10552034.

31. "Ansys Fluent User's Guide," Release 2023R2, (Ansys Inc., 2023), https://www.ansys.com/products/fluids/ansys-fluent.

32. "Ansys Fluent in Ansys Workbench User's Guide - Release 2023R2," (Ansys Inc., 2023), https://www.ansys.com/products/ansys-workbench.

33. M. Affenzeller, S. Winkler, S. Wagner, and A. Beham, "Genetic Algorithms and Genetic Programming - Modern Concepts and Practical Applications," in *Numerical Insights*, ed. A. Sydow (Taylor & Francis, 2009).

34. U. Stritzinger, W. Roland, G. Berger-Weber, and G. Steinbichler, "Modeling Melt Conveying and Power Consumption of Co-Rotating Twin-Screw Extruder Kneading Blocks: Part B. Prediction Models," *Polymer Engineering and Science* 63, no. 3 (2023): 841–862, https://doi.org/10.1002/pen.26249.

35. A. Hammer, W. Roland, C. Marschik, and G. Steinbichler, "Predicting the Co-Extrusion Flow of Non-Newtonian Fluids Through Rectangular Ducts — A Hybrid Modeling Approach," *Journal of Non-Newtonian Fluid Mechanics* 295 (2021): 104618, https://doi.org/10.1016/j.jnnfm.2021.104618.

36. H. Albrecht, W. Roland, C. Fiebig, and G. R. Berger-Weber, "Multi-Dimensional Regression Models for Predicting the Wall Thickness Distribution of Corrugated Pipes," *Polymers* 14, no. 17 (2022): 3455–3480, https://doi.org/10.3390/polym14173455.

37. S. Pachner, W. Roland, M. Aigner, C. Marschik, U. Stritzinger, and J. Miethlinger, "Using Symbolic Regression Models to Predict the Pressure Loss of Non-Newtonian Polymer-Melt Flows Through Melt-Filtration Systems With Woven Screens," *International Polymer Processing* 36, no. 4 (2021): 435–450, https://doi.org/10.1515/ipp-2020-4019.

38. W. Roland, M. Kommenda, C. Marschik, and J. Miethlinger, "Extended Regression Models for Predicting the Pumping Capability and Viscous Dissipation of Two-Dimensional Flows in Single-Screw Extrusion," *Polymers* 11, no. 2 (2019): 334–369, https://doi.org/10.3390/polym11020334.

39. C. Marschik and W. Roland, "Correction Factors for the Drag and Pressure Flows of Power-Law Fluids Through Rectangular Ducts," *Polymer Engineering and Science* 63, no. 7 (2023): 2043–2058, https://doi.org/10.1002/pen.26344.

40. D. Herzog, F. Lehner, W. Roland, C. Marschik, and G. Berger-Weber, "Impact of Domain Knowledge on Developing Pumping Models for Single-Screw Extruders Using Symbolic Regression," *International Polymer Processing* 40, no. 4 (2025): 439–456, https://doi.org/10.1515/ipp-2025-0021.

41. S. Wagner, G. Kronberger, A. Beham, et al., "Architecture and Design of the HeuristicLab Optimization Environment," in *Advanced Methods and Applications of Computational Intelligence*, ed. R. Klempous, J. Nikodem, W. Jacak, and Z. Chaczko (Springer, 2014), 197, https://doi.org/10.1007/978-3-319-01436-4.

42. H. Giesekus and G. Langer, "Die Bestimmung der wahren Fließkurven nicht-Newtonscher Flüssigkeiten und Plastischer Stoffe mit der Methode der repräsentativen Viskosität," *Rheologica Acta* 16 (1977): 1–22, https://doi.org/10.1007/BF01516925.

43. H. Potente, W. Hanhart, and T. Reski, "Design and Processing Optimization of Extruder Screws," *Polymer Engineering and Science* 34, no. 11 (1994): 937–945, https://doi.org/10.1002/pen.760341111.

44. K. Wilczyński, "Single-Screw Extrusion Model for Plasticating Extruders," *Polymer-Plastics Technology and Engineering* 38, no. 4 (1999): 581–608, https://doi.org/10.1080/03602559909351602.

45. A. R. Vincelette, C. S. Guerrero, P. J. Carreau, and P. G. Lafleur, "A Model for Single-Screw Plasticating Extruders," *International Polymer Processing* 4, no. 4 (1989): 232–241, https://doi.org/10.3139/217.890232.

46. W. Roland, C. Marschik, A. Hammer, and G. Steinbichler, "Modeling the Non-Isothermal Conveying Characteristics in Single Screw Extrusion by Application of Network Analysis," *SPE ANTEC Tech. Papers* 66 (2020): 388–395.

47. M. A. Spalding, G. A. Campbell, F. Carlson, and K. Nazrisdoust, "Using Extreme Barrel Diameters to Verify the Numerical Simulation of Single-Screw Extruders," *SPE ANTEC Tech. Papers* 52 (2006): 792–795.

48. C. Marschik, W. Roland, M. Dörner, G. Steinbichler, and V. Schöppner, "Leakage-Flow Models for Screw Extruders," *Polymers* 13, no. 12 (2021): 1919–1943, https://doi.org/10.3390/polym13121919.

Supporting Information

Additional supporting information can be found online in the Supporting Information section. **Data S1:** Analytical estimation of the relevance of viscoelastic effects on melt conveying. **Data S2:** Equations for the numerical grid parametrization used to conduct the flow simulations in ANSYS Fluent. **Data S3:** Scatter plots showing the value distribution of the original and transformed target variables. **Data S4:** Coefficients for the flight correction factors (Equations 34–36) used in the theoretical approximation equations. **Data S5:** Subfunctions and coefficients for the relative flow rate model (Equation 41). **Data S6:** Subfunctions and coefficients for the relative dissipation rate model (Equation 42). **Data S7:** Subfunctions and coefficients for the relative shear rate model (Equation 43). **Data S8:** Settings for the non-isothermal network analysis used to validate the melt conveying models experimentally.